

**COATING OF $\text{La}_{0.3}\text{Sr}_{0.7}\text{Fe}_{0.7}\text{Cr}_{0.3}\text{O}_{3-\delta}$ AND
 $\text{La}_{0.3}\text{Ca}_{0.7}\text{Fe}_{0.7}\text{Cr}_{0.3}\text{O}_{3-\delta}$ CATHODE LAYERS
ON GDC CERAMICS
BY ELECTROSPRAY DEPOSITION (ESD)**

**A Thesis Submitted to
the Graduate School of Engineering and Sciences of
İzmir Institute of Technology
in Partial Fulfillment of the Requirements for the Degree of
MASTER OF SCIENCE
in Materials Science and Engineering**

**by
Emre ERĐEN**

**July 2023
İZMİR**

We approve the thesis of **Emre ERĐEN**

Examining Committee Members:

Prof. Dr. Sedat AKKURT

Department of Materials Science and Engineering, İzmir Institute of Technology

Assoc. Prof. Umut ADEM

Department of Materials Science and Engineering, İzmir Institute of Technology

Assoc. Prof. Nesrin HORZUM POLAT

Department of Engineering Sciences, İzmir Kâtip Çelebi University

20 July 2023

Prof. Dr. Sedat AKKURT

Supervisor, Department of
Materials Science and Engineering,
İzmir Institute of Technology

Prof. Dr. Çekdar Vakıf AHMETOĐLU

Co-Supervisor, Department of
Materials Science and Engineering,
İzmir Institute of Technology

Prof. Dr. Sedat AKKURT

Head of the Department of
Materials Science and Engineering

Prof. Dr. Mehtap EANES

Dean of the Graduate School of
Engineering and Sciences

ACKNOWLEDGEMENTS

Firstly, I would like to thank and express my gratitude to my advisor, Prof. Dr. Sedat AKKURT. I am truly thankful for his invaluable guidance, advice, support, motivation, and encouragement throughout my thesis and my master's degree education in material science and engineering. I should sincerely admit that Prof. Akkurt holds a significant role in my academic journey as my advisor. It is an honor to work with him.

Secondly, I would like to thank my colleagues Tuğçe ÖZMEN EGESoy and Metin ÖZBEKLER for their support and friendship to improve my thesis.

I would like to thank Dr. Can SINDIRAÇ for guiding and helping our laboratory studies. I would like to thank Assoc. Prof. Aligül BÜYÜKAKSOY and his laboratory for the EIS measurements. I would also like to express my gratitude to the all lecturers and staff of IZTECH-CMR, especially Işın ÖZÇELİK and Zehra Sinem YILMAZ for their assistance.

Lastly, I wish to thank my beloved parents, Ulviye ERĞEN and Hamit ERĞEN, for their support, motivation, and trust in every step of my life. I would like to send my special thanks to my little sister, Zeynep ERĞEN. I'm thankful to my aunts, Hayriye YAŞLAK and Gülay YAŞLAK, who I know are always with me. I'm also appreciated for all my friends for sending me their best wishes.

ABSTRACT

COATING OF $\text{La}_{0.3}\text{Sr}_{0.7}\text{Fe}_{0.7}\text{Cr}_{0.3}\text{O}_{3-\delta}$ AND $\text{La}_{0.3}\text{Ca}_{0.7}\text{Fe}_{0.7}\text{Cr}_{0.3}\text{O}_{3-\delta}$ CATHODE LAYERS ON GDC CERAMICS BY ELECTROSPRAY DEPOSITION (ESD)

High temperatures are needed to rapidly transfer of O^{2-} ions between layers during the chemical energy to electrical energy conversion in solid oxide fuel cells (SOFC). Nevertheless, intermediate-temperature SOFCs are preferred to increase their lifetime and reduce maintenance and production costs. The performance of IT-SOFCs depends particularly on the microstructure and electrochemical properties of the cathode layer. In this study, cobalt-free $\text{La}_{0.3}\text{Sr}_{0.7}\text{Fe}_{0.7}\text{Cr}_{0.3}\text{O}_{3-\delta}$ and $\text{La}_{0.3}\text{Ca}_{0.7}\text{Fe}_{0.7}\text{Cr}_{0.3}\text{O}_{3-\delta}$ cathode layers were coated on GDC ceramic pellets by ESD method. The aim of the thesis was to have better structural and electrochemical properties of coatings than the literature. ESD provides the atomization of liquids with the help of electrical forces. ESD is an effective method for forming coatings with desired compositions. By changing ESD parameters, different structural properties such as reticular, cracked, and dense were obtained. Reticular structures are useful for easier oxygen transfer with increased surface area. Effects of parameters were examined by Plackett-Burman design, and the most effective parameter was found as flow rate. The quality of the coatings was evaluated by quantitative scoring. The 16th sample, which was coated with solution E, got the best score. Parameters of 16th sample were used in the investigation of the effects of different solutions on the coatings. 8 different solutions named A to H were prepared with different solvents and precursor salts. Coating by solution E shows better EIS results than the literature as $0.22 \Omega\cdot\text{cm}^2$. Coatings by solution G and A show close values to the literature as $0.29 \Omega\cdot\text{cm}^2$ and $0.34 \Omega\cdot\text{cm}^2$, respectively.

ÖZET

La_{0.3}Sr_{0.7}Fe_{0.7}Cr_{0.3}O_{3-δ} VE La_{0.3}Ca_{0.7}Fe_{0.7}Cr_{0.3}O_{3-δ} KATOT TABAKALARININ GDC SERAMİKLER ÜZERİNE ELEKTROPÜSKÜRTMEYLE BİRİKTİRME (ESD) İLE KAPLANMASI

Katı oksit yakıt hücrelerinde (KOYH) kimyasal enerjiden elektrik enerjisi dönüşümü sırasında katmanlar arası O²⁻ iyonlarının hızlı transferi için yüksek sıcaklıklara ihtiyaç duyulsa da kullanım ömürlerini arttırmak, bakım ve üretim maliyetlerini düşürmek için orta sıcaklık KOYH'ler tercih edilir. OS-KOYH'lerde performans, özellikle katot katmanının mikroyapısı ve elektrokimyasal özelliklerine bağlıdır. Kobalt içermeyen La_{0.3}Sr_{0.7}Fe_{0.7}Cr_{0.3}O_{3-δ} ve La_{0.3}Ca_{0.7}Fe_{0.7}Cr_{0.3}O_{3-δ} katot tabakaları ESD yöntemi ile GDC seramik peletler üzerine kaplanarak literatüre göre daha iyi yapısal ve elektrokimyasal özelliklere sahip olması amaçlanmıştır. ESD yöntemi, elektriksel kuvvetlerin yardımıyla sıvıların atomize edilmesini sağlamak ve istenilen bileşimlerde kaplamalar oluşturmak için etkili bir yöntem olduğu için tercih edilmiştir. ESD parametrelerinin değişimleriyle katot tabakasının mikroyapısı kontrol edilerek mercanimsi, çatlak ve yoğun gibi farklı yapı özellikleri elde edilmiştir. Mercanimsi yapıların en önemli avantajı, daha kolay oksijen transferinin ve daha verimli oksijen indirgeme reaksiyonlarının (ORR) yer alacağı yüzey alanlarının artırılmasıdır. Farklı parametre etkileri incelenmiş, deneysel tasarım yöntemi olan Plackett-Burmann yaklaşımı ile en etkili parametre akış hızı olarak bulunmuştur. Kaplamaların tercih edilen yapı özelliklerine göre uygunluğu, nicel puanlama ile değerlendirilmiştir. Buna göre en iyi puanı, E solüsyonu ile kaplanan 16. numune almıştır. Bu numunenin deneysel parametreleri farklı solüsyonların kaplama üzerindeki etkilerinin incelenmesi aşamasında kullanılmıştır. Bu aşamada farklı çözücüler ve öncül tuzlarla A'dan H'ye kadar isimlendirilen 8 farklı solüsyon hazırlanarak kaplamalar yapılmıştır. E, G ve A solüsyonları ile yapılan kaplamalardan elde edilen EIS ölçümleri sonucunda sırasıyla 0.22 Ω.cm², 0.29 Ω.cm² ve 0.34 Ω.cm² değerleri elde edilmiştir. Bu sonuçlar arasında E solüsyonu ile yapılan kaplamadan alınan ölçüm literatürden daha iyi, diğer kaplama ölçümlerinin ise literatüre yakın olduğu görülmüştür.

TABLE OF CONTENTS

LIST OF FIGURES	vii
LIST OF TABLES	x
CHAPTER 1. INTRODUCTION	1
1.1. Energy	1
1.2. Fuel Cells	2
1.2.1. Solid Oxide Fuel Cells.....	3
1.2.2. Problems with the use of Cobalt.....	6
1.3. Electro spray Deposition (ESD) Method	7
1.4. Electrochemical Impedance Spectroscopy (EIS).....	11
CHAPTER 2. EXPERIMENTAL PROCEDURE.....	14
2.1. Materials and Equipment	14
2.2. Statistical Experimental Design.....	19
2.3. Experimental Procedure.....	21
CHAPTER 3. RESULTS	26
3.1. Scoring of the Coatings.....	26
3.2. Significant Parameters w.r.t. Plackett-Burman Design	29
3.3. Chemical Analysis of Precipitates Obtained by Evaporation of the Solutions	31
3.4. Ladder Design Experiments for the Effect of Flow Rate	33
3.5. Coating Structure as Observed from Top View.....	35
3.6. Average Thickness of Coatings	40
3.7. X-Ray Diffraction Analysis of Coatings	43
3.8. Electrochemical Impedance Spectroscopy (EIS) Results	48
CHAPTER 4. CONCLUSION	59
REFERENCES	61

LIST OF FIGURES

<u>Figure</u>	<u>Page</u>
Figure 1.1. Schematic of Working principle of SOFC.....	4
Figure 1.2. Global Cobalt Production in 2021.....	7
Figure 1.3. Schematic of the ESD setup used in this study	8
Figure 1.4. Electrospraying Modes.....	8
Figure 1.5. Taylor Cone on Needle Tip.....	9
Figure 1.6. The needle and the target.....	10
Figure 2.1. GDC Pellets.....	14
Figure 2.2. Cylindrical Stainless-steel Mold	15
Figure 2.3. Single-axis Hydraulic Press (Carver Hydraulic Press, Wabash, IN, USA)..	15
Figure 2.4. Laboratory Box Kiln (Nabertherm LHT 02/17, Germany).....	16
Figure 2.5. SEM Image of GDC Powder	17
Figure 2.6. Particle Size Distribution from Producer Website	17
Figure 2.7. Particle Size Distribution Histogram	18
Figure 2.8. ESD Setup	19
Figure 2.9. Schematic of Experimental Method	21
Figure 2.10. Temperature vs Time Graph of Sintering Process	22
Figure 2.11. SEM Image of Dense GDC Ceramic Pellet After Sintering Process	22
Figure 2.12. XRD Peaks of GDC Pellet	23
Figure 3.1. Example of Score 1 with Experiment 15.....	26
Figure 3.2. Example of Score 2 with Experiment 14.....	27
Figure 3.3. Example of Score 3 with Experiment 11	27
Figure 3.4. Example of Score 4 with Experiment 4.....	28
Figure 3.5. Example of Score 5 with Experiment 3.....	28
Figure 3.6. SEM Image of homogeneous coating distribution on Experiment 3	35
Figure 3.7. SEM Image of non-homogeneous coating distribution on Experiment 15 ..	36
Figure 3.8. SEM Image of Coated GDC Pellet by Solution A	36
Figure 3.9. SEM Image of Coated GDC Pellet by Solution B	37
Figure 3.10. SEM Image of Coated GDC Pellet by Solution C	37

<u>Figure</u>	<u>Page</u>
Figure 3.11. SEM Image of Coated GDC Pellet by Solution D	38
Figure 3.12. SEM Image of Coated GDC Pellet by Solution E	38
Figure 3.13. SEM Image of Coated GDC Pellet by Solution F	39
Figure 3.14. SEM Image of Coated GDC Pellet by Solution G	39
Figure 3.15. SEM Image of Coated GDC Pellet by Solution H	40
Figure 3.16. Cross-sectional SEM Image of Coated GDC Pellet by Solution D	41
Figure 3.17. Cross-sectional SEM Image of Coated GDC Pellet by Solution E	42
Figure 3.18. Cross-sectional SEM Image of Coated GDC Pellet by Solution F	42
Figure 3.19. XRD Analysis Chart of Coating made by Solution A	43
Figure 3.20. XRD Analysis Chart of Coating made by Solution B	44
Figure 3.21. XRD Analysis Chart of Coating made by Solution C	44
Figure 3.22. XRD Analysis Chart of Coating made by Solution D	45
Figure 3.23. XRD Analysis Chart for (a) coating made by Solution E on GDC Pellet, (b) scraped coating made by Solution E and separately heated at 700 °C for 2 hours	46
Figure 3.24. XRD Analysis Chart of Coating made by Solution E	46
Figure 3.25. XRD Analysis Chart of Coating made by Solution F	47
Figure 3.26. XRD Analysis Chart of Coating made by Solution G	47
Figure 3.27. XRD Analysis Chart of Coating made by Solution H	48
Figure 3.28. a) Impedance response of the symmetrical half cells with sample 16 electrodes, collected at 700 °C, in stagnant air. Equivalent circuit used to fit the impedance data is also provided above the Nyquist and Bode plots. b) Temperature dependence of the area specific resistance components of the overall impedance response, namely ASR1, ASR 2, and ASR 3	52
Figure 3.29. ASR _{electrode} Values of Symmetrical Half Cell Coated with Solution A	53
Figure 3.30. Nyquist Plot of 700 Up Process in EIS with Solution A Coated Symmetrical Half Cell	53
Figure 3.31. Bode Plot of 700 Up Process in EIS with Solution A Coated Symmetrical Half Cell	54

<u>Figure</u>	<u>Page</u>
Figure 3.32. $ASR_{\text{electrode}}$ Values of Symmetrical Half Cell Coated with Solution B	54
Figure 3.33. $ASR_{\text{electrode}}$ Values of Symmetrical Half Cell Coated with Solution C	55
Figure 3.34. $ASR_{\text{electrode}}$ Values of Symmetrical Half Cell Coated with Solution D	55
Figure 3.35. $ASR_{\text{electrode}}$ Values of Symmetrical Half Cell Coated with Solution F	56
Figure 3.36. $ASR_{\text{electrode}}$ Values of Symmetrical Half Cell Coated with Solution G	56
Figure 3.37. Nyquist Plot of 700 Down Process in EIS with Solution G Coated Symmetrical Half Cell	57
Figure 3.38. Bode Plot of 700 Down Process in EIS with Solution G Coated Symmetrical Half Cell	57
Figure 3.39. $ASR_{\text{electrode}}$ Values of Symmetrical Half Cell Coated with Solution H	58

LIST OF TABLES

<u>Table</u>	<u>Page</u>
Table 2.1. High and Low Levels of Selected Factors for Plackett-Burman screening design.....	20
Table 2.2. Experimental design layout for Plackett–Burman approach	20
Table 2.3. Solvent Types	24
Table 2.4. Precursor Salts.....	24
Table 2.5. Content of Solutions	25
Table 3.1. Experiments designed via Plackett–Burman approach	29
Table 3.2. Evaluation of the Plackett-Burman Design	30
Table 3.3. EDX Results of Solutions A and E	31
Table 3.4. EDX Results of Solutions C and G.....	31
Table 3.5. EDX Results of Solutions B and F	32
Table 3.6. EDX Results of Solutions D and H.....	32
Table 3.7. Calculated Stoichiometric Proportions of Solutions	33
Table 3.8. Flow Rate Difference in SEM Images	33
Table 3.9. Average Thickness of Coatings on Second Part Experiments	41
Table 3.10. Summary of area specific resistance, capacitance and summit frequency. Errors associated with the ASR, P and n parameters determined through the equivalent circuit fittings were below 15%.....	51
Table 3.11. Obtained ASR _{electrode} Values by Samples A to H	52

CHAPTER 1

INTRODUCTION

In the Introduction part, energy needs, fuel cells, solid oxide fuel cells, cobalt-related problems in the cathode layers of solid oxide fuel cells and electrospray deposition (ESD) method are explained. In these sections, information from the literature is also included besides the thesis details. Thesis studies were carried out in line with the developable areas in literature search.

1.1. Energy

Technological developments, industrialization and growing world population increase the energy demand rapidly. Energy, is used in almost every field of daily life, is a necessary element for increasing the welfare level of societies. Energy can be found in different types such as mechanical, heat, electrical, chemical and nuclear. Energy can be transformed from one type to another by appropriate methods and it can be classified in different ways. According to the classification made by their use, energy resources are divided into two parts as renewable and non-renewable. Water, solar, wind, geothermal, biomass, wave tide, hydrogen are renewable energy sources while coal, petroleum, natural gas, uranium, etc. are considered as non-renewable energy sources ^[1]. The world's energy needs gradually increase due to the increasing population and technological developments. In order to encounter the need, the use of non-renewable energy resources with limited reserves should be planned and the use of renewable energy resources should be increased and developed ^[2].

More energy use means more carbon emissions. Ultimately, this process causes environmental pollution ^[3]. The damage caused by carbon emissions to the environment has reached significant dimensions. A large part of carbon emissions originate from the use of fossil resources in the energy sector, and as energy consumption increases, carbon emissions also increase. After the use of fossil resources, they release harmful gases to the environment such as direct greenhouse gases (CO₂) and indirect greenhouse gases such as nitrogen oxides (NO_x), carbon monoxide (CO) and sulfur dioxide (SO₂). The

greenhouse effect, which causes climate change, occurs with the increase in the concentration of these released gases in the atmosphere ^[4]. To prevent these types of problems, increasing the use of renewable energy sources is necessary. In addition, efforts have been made around the world to reduce carbon footprint. The European Union Commission prepared the EU Green Deal protocol in 2019 on the against climate change ^[5]. Now the FitFor55 package, which includes the necessary regulations and regulations, have been put into effect. The package, which aims to reduce global greenhouse gas emissions by 55 percent until 2030, includes sanctions such as imposing additional taxes on industrial products based on carbon emissions, imposing a carbon tax at the border, and tightening air and sea transportation controls ^[6]. Within the scope of the Carbon Border Adjustment Mechanism (CBAM) system, the European Union primarily aimed to prevent carbon leakage and to impose additional taxation on imported products in some sectors according to carbon rates ^[7]. Also, REPowerEU plan is presented in 2022 by EU to produce clean energy, expedite transition, save energy, vary the types of sources ^[6]. Hydrogen has the highest energy content per unit mass among all known fuels, it makes hydrogen one of the most efficient alternative fuels (Calorific value of hydrogen is between 120.7-140.9 MJ/kg.) ^[8,9]. The plans which aim to increase use of renewable resources, also aim to develop the hydrogen technologies.

1.2. Fuel Cells

Traditional power generation systems use combustion reactions first to convert the energy in the fuel into electricity. The fuel and oxidizer (oxygen) must be mixed thoroughly for an efficient process. Some intermediate processes are required until electrical energy is produced, and each intermediate process can lead to energy loss, thus reducing efficiency ^[10]. In fuel cells, the fuel is directly converted into electrical energy. Unlike traditional production systems, fuel and oxygen do not mix, which allows the system to work more efficiently. Fuel cells are divided into three groups according to their operating temperatures as low, medium and high temperature fuel cells. Operating temperatures are classified as 100°C-300°C for low temperature fuel cells, 300°C-700°C for intermediate temperature fuel cells and 700°C-1000°C for high temperature fuel cells. However, the classification based on electrolyte type instead of operating temperature is more common. Fuel cells take various names according to their electrolyte type like direct

methanol fuel cells (DMFC), alkaline fuel cells (AFC), phosphoric acid fuel cells (PAFC), proton-exchange membrane fuel cells (PEMFC), molten carbonate fuel cell (MCFC) and solid oxide fuel cells (SOFC) ^[11].

1.2.1. Solid Oxide Fuel Cells

Solid oxide fuel cells (SOFCs) are high-efficiency electrochemical devices that can convert chemical energy into electricity ^[10]. They also have environmental advantages such as low NO_x and SO_x pollutant emission values. Fuel flexibility, higher energy efficiency, long lifetimes, higher mechanical strength, thermal stability, modularity, scalability, silent operation and operating without precious metals as catalysts can be listed as other outstanding features of SOFCs by comparison with other energy conversion devices ^[10,12]. Although the working principle of solid oxide fuel cells is quite similar to batteries, they do not need to be recharged. They continue to work as long as they are fed with oxygen and hydrogen ^[13]. A classical SOFC have porous anode electrode/ dense ceramic electrolyte / porous cathode electrode structure. Fuel feeds the anode part of the SOFC. Anode layer can be named as fuel electrode. The oxidation reaction takes place at the anode and the electrons move through the open circuit. At the cathode, electrons come from the open circuit and perform the reduction reaction. Cathode layer can be named as oxygen (air) electrode. Electricity is produced when transferring electrons from the anode to the cathode on the open circuit as schematically shown in Figure 1.1. There is only water and heat output while generating electrical energy, while no additional substances polluting the nature are released ^[14-16]. Good ionic conductivity is required to facilitate the passage of oxygen ions in the electrolyte. The electronic conductivity of the electrolyte should be low to prevent short circuit formation during electron transfer ^[17]. The anode layer must provide a compatible environment for sufficient catalytic activity for the oxidation of the fuel. The anode layer must also have high ionic conductivity in order to ensure that the oxygen ions that are reduced at the cathode and passed through the electrolyte are dispersed at the anode/electrolyte interface ^[18,19]. The cathode layer reduces the oxygen gas coming from outside to O²⁻. The cathode material must have good both electronic and ionic conductivity in the oxidizing environment. At the same time, it should be in a porous (reticular) structure for the

transmission of oxygen gas. For these reasons, the cathode layer determines the performance of a SOFC [20].

The reactions in layers of a classical SOFC are given below: [21]:

- Anode: $\text{H}_2 + \text{O}^{2-} \rightarrow \text{H}_2\text{O} + 2\text{e}^-$
- Cathode: $\frac{1}{2}\text{O}_2 + 2\text{e}^- \rightarrow \text{O}^{2-}$
- Total: $\text{H}_2 + \frac{1}{2}\text{O}_2 \rightarrow \text{H}_2\text{O}$

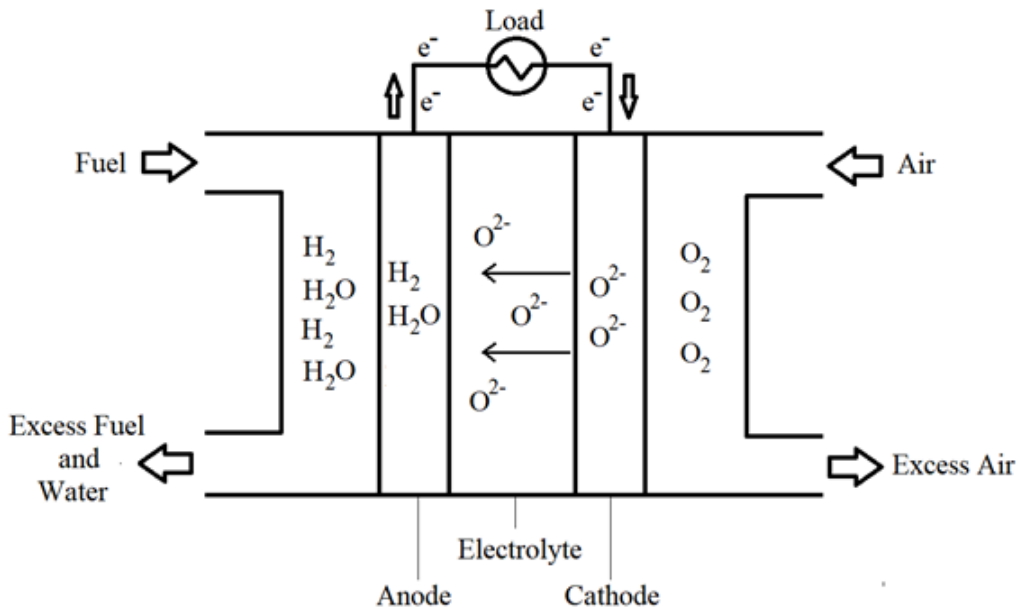


Figure 1.1. Schematic of working principle of SOFC

High temperatures (800-1000 °C) are needed for the rapid diffusion of O²⁻ ions in the anode, electrolyte and cathode layers, and SOFCs are operated at these high-temperature levels. Typical solid oxide fuel cell consists of yttria-stabilized zirconia (YSZ) electrolyte, Ni-YSZ composite as fuel electrode, and lanthanum strontium manganite (LSM) - YSZ composites as air electrodes and require especially high operating temperature (800-1000 °C) [22,23]. Operation of SOFCs at these high temperatures is costly and maintenance demanding. These reasons slow down the commercialization of SOFC technology [24]. Therefore, lowering the high operating temperature to 500-700 °C is necessary to increase the expected lifetime, reduce operating costs, shorten start-up time, and take advantage of a wide variety of material options such as metallic interconnect materials (Fe-Cr alloy) to replace expensive ceramic materials [25,26]. In addition, this high temperature can significantly compromise cell performance by causing sulfur poisoning and coking [27,28]. In addition, Ni coarsening is another

important problem during long-term operation, as it causes a reduction in the length of the three-phase boundary (TPB) where the electrode, electrolyte and gas phases meet and redox reactions take place ^[29,30]. $\text{La}_{1-x}\text{Sr}_x\text{MnO}_3$ (LSM) electrodes can be separated from the electrolyte layer during oxygen formation ^[29]. For all these reasons, Ni-YSZ/YSZ/LSM-YSZ materials should be replaced with new materials. Using an electrolyte with higher ionic conductivity such as gadolinium-doped ceria (GDC) and samarium-doped ceria (SDC) instead of conventional yttrium-stabilized zirconia (YSZ) at medium operating temperature has proven successful ^[31]. GDC ($\text{Ce}_{0.9}\text{Gd}_{0.1}\text{O}_{1.9}$) electrolytes were used in the thesis. The doping process is applied to improve the properties of the compound. Gd was added to cerium oxide at a 10% molar ratio to increase the oxygen vacancies. Lowering operating temperatures can have several disadvantages about the performance. There are various ideas for eliminating these disadvantages. These ideas are reducing the thickness of the electrolyte for shortening the transporting distance of oxygen ions to minimize ohmic losses, using electrolyte materials with high ionic conductivity at intermediate temperature levels, using MIEC (Mixed Ionic-Electronic Conductor) materials instead of conventional cathodes with low oxygen reduction kinetics, and manufacturing fuel cell layers by thin film methods. The most widely used cathode MIEC materials in the last decade is $\text{La}_{1-x}\text{Sr}_x\text{Co}_{1-y}\text{Fe}_y\text{O}_{3-d}$ (LSCF) due to its high ionic-electrical conductivity and catalytic activity towards oxygen reduction ^[30,31]. However, LSCF has a coefficient of thermal expansion that is significantly higher than that of the GDC electrolyte material. Also, its chemical stability under operating conditions is insufficient ^[32,33]. The main factor of these disadvantages is related to the presence of Co(IV)/Co(III) in its structure ^[34]. Eliminating problems associated with the use of cobalt in SOFCs was mentioned in (Title 1.2.2.). Electro spray deposition is an easy and efficient technique for the fabrication of electrode layers that does not require vacuum conditions. In addition, ESD provides control of the microstructure, which helps to improve the performance of SOFC. Djurado et al. ^[35-42] studied the effects of electro spraying parameters on the microstructure of LSCF cathode layers. Sındıraç et al. ^[43] also studied similar cathode layers with different solvents. It has been reported that cathode layers with a reticular structure can be coated on GDC electrolytes with a solution containing ionic mixtures formed with cathode compositions by using the ESD method. The reticular structure is preferred because of the surface area it offers for the oxygen reduction reaction (ORR) and easy access to the triple-phase boundaries (TPB) of oxygen. There is a lot of interest in the development of symmetrical

SOFCs, which use the same redox stable materials on the anode and cathode layers to increase lifetime, reduce voltages, and reduce cost [32]. The use of the same anode and cathode compositions in SOFCs leads to reduced production costs with the ease of co-sintering. These symmetrical SOFCs can be operated as reversible SOFCs. In this study, LSFcr, which was used as the electrode material, was coated both sides symmetrically.

1.2.2. Problems with the use of Cobalt

Cobalt-containing perovskite cathode materials have critical disadvantages such as the high coefficient of thermal expansion (CTE), unsatisfactory chemical and mechanical stabilities in long-term use, relatively high cost, etc. In the last 15 years, new cobalt-free cathode materials were researched to eliminate problems associated with the use of cobalt in SOFCs. To improve mechanical and chemical stability, cobalt-free MIEC materials have been extensively researched over the past 15 years. Chen et al. [32] investigated $\text{La}_{0.3}\text{Sr}_{0.7}\text{Fe}_{1-y}\text{Cr}_y\text{O}_{2-d}$ (LSFCr) for the first time in the literature. This material exhibited good catalytic activity during the oxidation of fuels and provided high redox stability. Also, replacing Co with Cr resulted in a reduction in the coefficient of thermal expansion from $23.0 \times 10^{-6} \text{ K}^{-1}$ to $20.9 \times 10^{-6} \text{ K}^{-1}$ at $700 \text{ }^\circ\text{C}$, respectively. The closer CTE values eliminate the mismatches that will occur between the electrode and the electrolyte. This value is closer to the thermal expansion coefficient of GDC ($12.7 \times 10^{-6} \text{ K}^{-1}$). Various fabrication techniques have been used to prepare reversible solid oxide fuel cells with LSFcr. Researches are being made to increase the performance of SOFCs and to ensure stability. However, only limited production techniques can be applied [33,34,44-47] and there are areas for improvement. Çelikbilek et al. [48] showed that LSCF cathode layers produced by ESD (Electrospray Deposition) showed the lowest area-specific resistivity (ASR) value among other methods with the same stoichiometry at intermediate temperature. In addition, Kozokaro et al. [46] studied catalytic properties of $\text{La}_{0.3}\text{Sr}_{0.7}\text{Fe}_{0.7}\text{Cr}_{0.3}\text{O}_{3-\delta}$ with using density functional theory (DFT). $\text{Pr}_{0.7}\text{Ca}_{0.3}\text{Cr}_{1-y}\text{Mn}_y\text{O}_{3-\delta}$, $(\text{La}_{0.6}\text{Sr}_{0.4})_{0.98}\text{FeO}_{3-\delta}$, $\text{BaFe}_{0.7}\text{Zr}_{0.2}\text{Y}_{0.1}\text{O}_{3-\delta}$, $\text{Ba}_{1-x}\text{Nd}_x\text{FeO}_{3-\delta}$, $\text{La}_{0.75}\text{Sr}_{0.2}\text{Cr}_{0.5}\text{X}'_{0.5}\text{O}_{3-\delta}$ ($\text{X}' = \text{Mn, Fe and Al}$), $\text{La}_{0.9}\text{Sr}_{0.1}\text{Ga}_{0.8}\text{Mg}_{0.2}\text{O}_{2.85}$ (LSGM), etc. materials are used in literature in recent years [49-57]. The $\text{La}_{0.3}\text{Sr}_{0.7}\text{Fe}_{0.7}\text{Cr}_{0.3}\text{O}_{3-\delta}$ and $\text{La}_{0.3}\text{Ca}_{0.7}\text{Fe}_{0.7}\text{Cr}_{0.3}\text{O}_{3-\delta}$ electrodes were produced by ESD in this thesis.

There are also socioeconomic aspects for replacement of cobalt in SOFC materials. Bamana et al studied cobalt mining in the Democratic Republic of the Congo [58]. They indicated that cobalt mining was accompanied by violence, food and water insecurity, substance abuse, and physical and mental health challenges. Moreover, Congolese people have lost their farmland and homes. Another study [59] showed that people living around the town of Kolwezi had much higher levels of cobalt in their urine and blood than people living in a nearby control area. That study reveals toxic harm to vulnerable communities due to cobalt mining. Although cobalt is a unique base metal used in many applications, its supply is dominated by a single country, the Democratic Republic of Congo (DRC), which produces about 72% of worldwide cobalt with no other country producing more than 5% in 2021 as shown in Figure 1.2 [60-62]. Due to the high cost and price volatility associated with cobalt, manufacturers investigate alternatives to reduce or eliminate the need for cobalt in applications especially in batteries production [63,64]. For all those reasons, it is obvious that the currently existing cobalt supply chain is not sustainable and the use of cobalt in critical applications for daily life needs to be lowered [59,65].

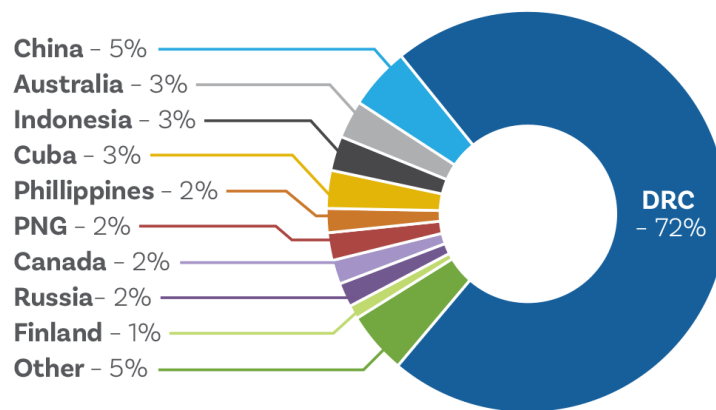


Figure 1.2. Global Cobalt Production in 2021 [62]

1.3. Electrospray Deposition (ESD) Method

Electrospray deposition method is applied for the cathode layer coatings within the study of thesis. In this title, theory of the ESD and the important points of the method are explained. This method is applied by spraying a solution under high voltage onto the ceramic electrolyte as shown schematically in Figure 1.3 [66].

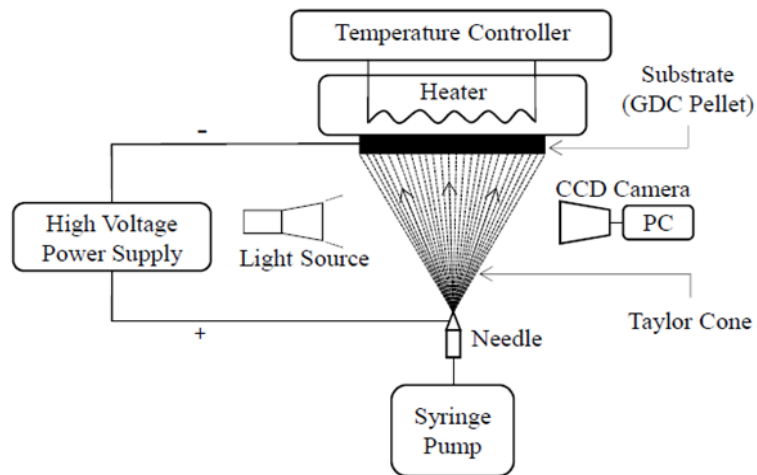


Figure 1.3. Schematic of the ESD setup used in this study ^[66]

The manner in which the aerosol is dispersed by the electrical field relies on factors such as the voltage applied, the flow rate, and the characteristics of the liquid. Various spraying modes are shown in the Figure 1.4. Among the different modes of electrospaying, the cone-jet mode is highly favored due to its ability to produce droplets of uniform size ranging from a few micrometers. Cone-jet mode is formed by the continuation of Taylor Cone which occurs at the needle tip.

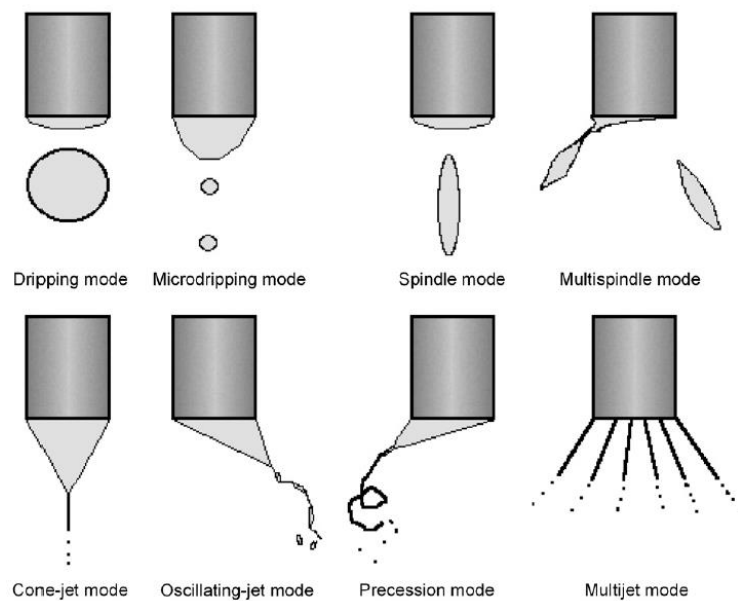


Figure 1.4. Electrospaying Modes ^[67]

The solution is expected to form a Taylor cone as it travels from the needle tip to the aluminum plate as shown in Figure 1.5. The solution becomes a spray form, and it is distributed homogeneously to every area of GDC pellet and aluminum plate as shown in Figure 1.6. The liquids in the solution evaporate on the ceramic pellet, which is heated to a temperature higher than the evaporation temperature of the components of the solution. The salts in the solution adhere to the ceramic and the coating process is completed.

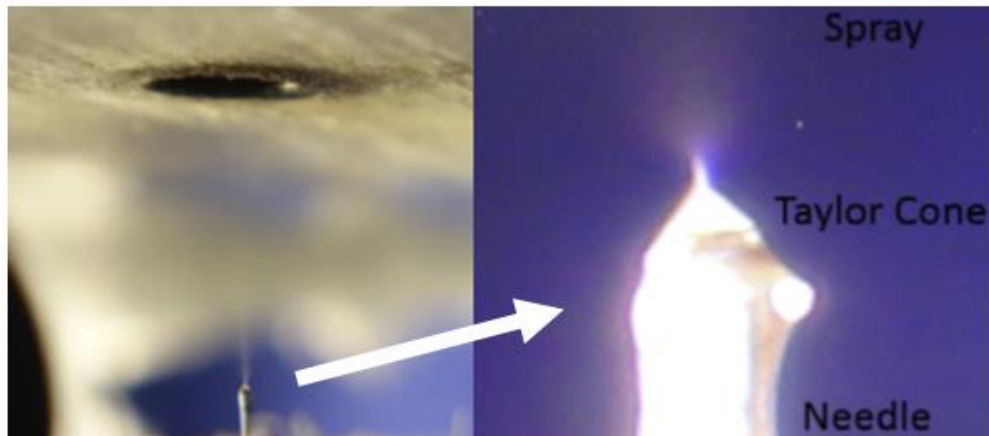


Figure 1.5. Taylor Cone on Needle Tip

Since the electric field is applied, the method is called electrospray deposition or ESD shortly. The electrospray deposition setup is shown schematically in Figure 1.3. It is a low-cost coating method that provides optimization of the microstructure by changing the sputtering parameters. Flow rate, solution concentration, voltage, working distance, substrate temperature can be listed as examples of experimental parameters. The advantages of the ESD technique are that it has a simple and low-cost installation, being a fast method, control of the stoichiometry in solutions, and the ability to control properties of deposited layers.

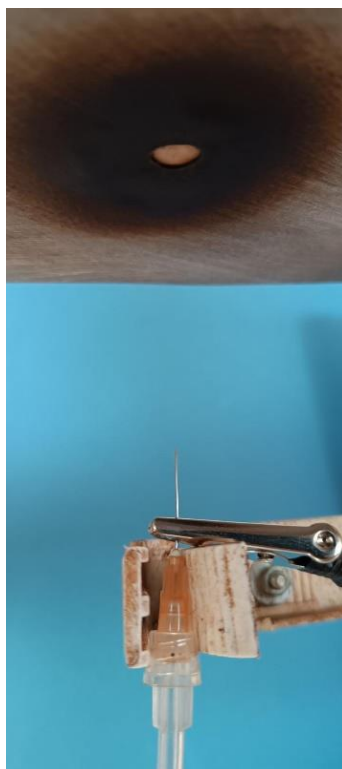


Figure 1.6. The needle and the target

One of the aims of this thesis is the optimization of ESD parameters. Each parameter can make the properties of coatings improve or worsen. When the working distance is increased, a significant portion of the solvent evaporates, causing the droplets to decrease in size. The resulting drier droplets, upon reaching the substrate, form a deposition layer that is more packed and denser. If there is enough solvent in the droplet, it will strike the ceramic surface with electrical force and spread over the surface. If the working distance is close, cracked and porous structure may be observed during the evaporation and drying of solvents since the amount of solvent in the droplet will be high. If the distance is far, the solvents will evaporate before they reach the ceramic and it will be difficult for the coating to spread and adhere. Flow rate affects the initial droplet size at the needle tip. Thus, the size of the droplets that will fall on the ceramic varies with the flow rate. According to the determined working distance, large droplets should be formed so the flow rate should be increased and the droplet does not dry totally. According to the statistical calculations made in Results 3.1, it was determined that the most important factor affecting the coating structure was the flow rate. In addition, the change of coating thickness by changing the flow rate was also examined in thesis. Temperature is effective in the evaporation of solvents when droplets come to the surface. In addition, the droplets

are exposed to this temperature during flight due to the transportation of the heat from the heater to air. Since the spreading of the incoming particles when they hit the surface is quicker than the evaporation of the solvents, the coating is expected to thicken as the coating time increases. The concentration of solution is related to the amount of particles that staying and coating on the surface by the evaporation of the solvents in the droplet. The flight times of the droplets change with the applied voltage. If the voltage increases more than necessary, the droplets coming out of the needle tip immediately hit the surface and a short circuit-like situation occurs. Also, no cone formation was observed in such a case.

1.4. Electrochemical Impedance Spectroscopy (EIS)

Electrochemistry is a field that covers a wide range of chemical reactions involving the transfer of electrons, homogeneous reactions occurring at electrodes surfaces, properties of electrolytes, etc. Electrochemical reactions take place in numerous research fields such as energy storage, energy conversion, sensors, biosensing applications, corrosion, etc. In the direction of these research fields, techniques like scanning electrochemical microscopy, cyclic voltammetry, chronopotentiometry, chronoamperometry and electrochemical impedance spectroscopy (EIS) are favored ^[68]. Electrochemical impedance spectroscopy (EIS) is a technique used to analyze the electrical behavior of electrochemical systems. It involves applying an alternating current (AC) signal to an electrochemical cell or system and measuring the resulting impedance response. Impedance refers to the combined resistance and reactance of a system to the AC signal. In EIS, a range of AC frequencies is typically applied, and the resulting impedance is measured. By analyzing the impedance data, valuable information about the electrochemical processes occurring within the system can be obtained ^[69]. EIS can provide insights into parameters such as the electrolyte resistance, charge transfer resistance, double-layer capacitance, and diffusion characteristics of the species involved. EIS is widely used in various fields, including corrosion studies, battery characterization, fuel cell analysis, sensor development, and material characterization ^[68]. It offers a powerful tool for understanding and studying the electrochemical behavior of systems and materials. Frequency range, electrode configuration, electrolyte composition, electrode materials, and data analyses are some key considerations about EIS

measurements. EIS can be used as a diagnostic tool to assess the performance and degradation of SOFCs. By monitoring changes in impedance over time, it is possible to detect and analyze processes such as electrode degradation, gas crossover, and changes in the electrochemical reaction kinetics that may affect the cell's long-term stability and efficiency. EIS is a valuable technique for investigating the electrochemical behavior, performance, and degradation mechanisms of solid oxide fuel cells [70]. It provides important insights into the various processes occurring within SOFC components, aiding in their optimization and advancement as efficient and sustainable energy conversion devices.

EIS measurement results are expressed intelligibly in the forms of Bode and Nyquist plots. Bode plots are commonly used in electrochemical impedance spectroscopy (EIS) measurements for analyzing the impedance response of a system as a function of frequency. Bode plots display both the magnitude and phase of the impedance, allowing for a comprehensive understanding of the system's behavior. Bode plots are utilized as magnitude and phase plots. The magnitude bode plot represents the absolute value of the impedance ($|Z|$) on the y-axis, typically plotted on a logarithmic scale, against the logarithm of the frequency ($\log(f)$) on the x-axis [69]. This plot provides information about the magnitude of the impedance response at different frequencies. Peaks or characteristic patterns in the magnitude plot can indicate specific electrochemical processes or phenomena occurring within the system. For example, in solid oxide fuel cells, peaks in the magnitude plot may correspond to electrode polarization or mass transport limitations [70]. The phase bode plot represents the phase angle of the impedance (θ) on the y-axis, usually plotted against the logarithm of the frequency ($\log(f)$) on the x-axis. The phase angle indicates the time delay between the applied AC signal and the system's response. It provides insights into the phase relationship between the voltage and current in the system. The phase plot can help identify the presence of capacitive, resistive, or inductive behavior in the system. For instance, in EIS measurements of batteries, the phase plot can reveal the presence of charge transfer reactions or diffusion processes. In summary, bode plots in EIS measurements provide valuable visual representations of the impedance response of a system, enabling researchers to analyze and interpret the electrochemical behavior across different frequencies. Nyquist plots are commonly used in electrochemical impedance spectroscopy (EIS) measurements to analyze the impedance response of a system in the complex plane. Nyquist plots provide a graphical representation of the impedance, with the real component (Z') plotted on the x-axis and

the imaginary component (Z'') plotted on the y-axis ^[69]. Nyquist plots are used in EIS measurements for the representation of impedance, identification of electrochemical processes, equivalent circuit analyses, evaluation of system performance, interpretation of impedance spectra, etc. Nyquist plots display the impedance response of a system as a series of points or a curve in the complex plane. Each point or data point on the plot corresponds to the impedance magnitude and phase at a specific frequency. The shape and pattern of the Nyquist plot can provide insights into the electrochemical processes occurring within the system. Different regions or features in the Nyquist plot represent specific electrochemical processes. Nyquist plots can be analyzed using equivalent circuit models to extract quantitative parameters related to the electrochemical system. By fitting the experimental data to a suitable equivalent circuit model, information about the resistance, capacitance, and inductance components of the system can be obtained. This allows for a more detailed understanding of the electrochemical behavior and enables comparison with theoretical predictions. Nyquist plots can be used to assess the performance and characteristics of electrochemical systems. Nyquist plots provide a visual representation of the entire impedance spectrum obtained from EIS measurements. Nyquist plots are widely used and offer a powerful tool for analyzing and interpreting the impedance response in EIS measurements ^[68]. They provide a comprehensive visualization of the impedance behavior in the complex plane, enabling researchers to study electrochemical processes, evaluate system performance, and extract valuable quantitative information.

CHAPTER 2

EXPERIMENTAL PROCEDURE

In this section, materials and equipment, statistical experiment design, experimental procedure will be explained. The properties of the test materials, the preparation of the test samples, the preparation of the test plans, the conditions of the experiments are expressed.

2.1. Materials and Equipments

Ceramic electrolyte pellets were prepared using gadolinia doped ceria powder shown in Figure 2.1 (GDC, $\text{Ce}_{0.9}\text{Gd}_{0.1}\text{O}_{3-\delta}$, Fuelcellmaterials, FCM, >99%). These pellets were formed into a cylindrical stainless-steel mold with a 15 mm inner diameter shown in Figure 2.2 by uniaxial pressing (Carver Hydraulic Press, Wabash, IN, USA) at 180 MPa pressure, shown in Figure 2.3. Pellet heights were approximately 1 mm. These pressed pellets were sintered in an electrically heated laboratory kiln (Nabertherm LHT 02/17, Germany) shown in Figure 2.4 with a residence time of 8 hours at 1400 °C and a heating/cooling value of 3 °C/min. The density of the prepared pellets is greater than 95% as measured by the Archimedes Method ^[71].



Figure 2.1. GDC Pellets



Figure 2.2. Cylindrical Stainless-steel Mold



Figure 2.3. Single-axis Hydraulic Press (Carver Hydraulic Press, IN, USA)



Figure 2.4. Laboratory Box Kiln (Nabertherm LHT 02/17, Germany)

Gadolinia-doped ceria is preferable material with its good ionic conductivity around $5 \times 10^{-3} \text{ S.cm}^{-1}$ at $500 \text{ }^\circ\text{C}$ [72,73]. GDC has cubic fluorite structure and Fm-3m space group. It has $5.8 \text{ m}^2/\text{g}$ surface area as located on product packaging and a crystallographic density as 7.2 g/cm^3 [74]. The SEM image of GDC Powder is shown in the Figure 2.5. The freeware named as ImageJ (Image Processing and Analysis in Java, National Institute of Health, USA) was used to measure particle sizes on the SEM image (dimensions: 1536×1103) of GDC powder. The scale bar is 500 nm on SEM image and it is known distance for converting pixels to nm. Thanks to ImageJ, the scale bar was measured and the value was entered to Set Scale option. In this way, all measurements of GDC particles on image was measured in accordance with scale bar. In addition, particle size distribution studies have been carried out with this method in the literature [75-77].

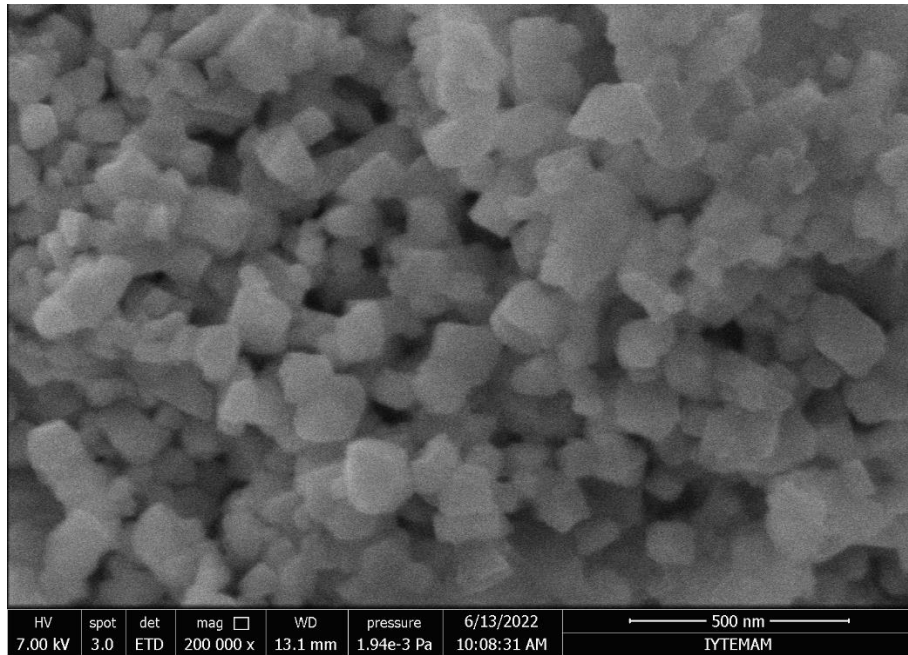


Figure 2.5. SEM Image of GDC Powder

GDC has particle diameter vs. distribution by volume (percent) graph on product website as shown in Figure 2.6. According to the measurements made, the histogram in the Figure 2.7 was obtained. Although D_{50} in volume distribution is $0.20\ \mu\text{m}$ from this graph, average particle size (D_{50}) value of GDC on product property paper is specified as $0.1 - 0.4\ \mu\text{m}$ [78]. The value I found is $0.14\ \mu\text{m}$, and it also takes place between this range. In addition, all measurements were also within this range as seen on histogram, no different results were encountered.

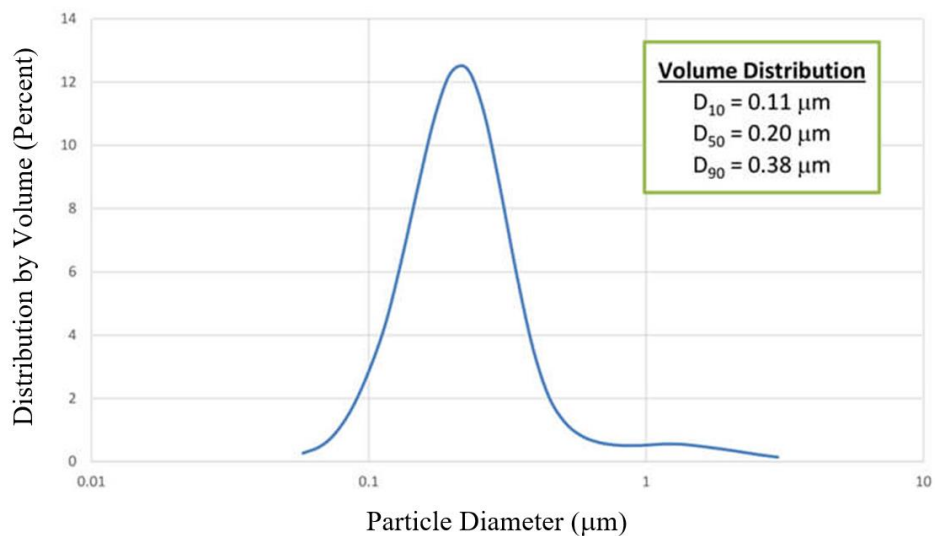


Figure 2.6. Particle Size Distribution from Producer Website [78]

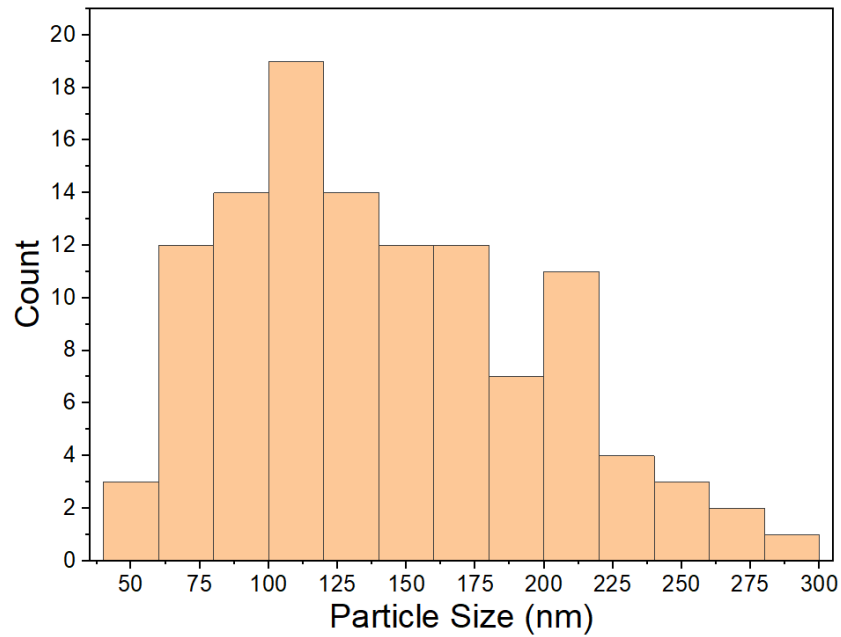
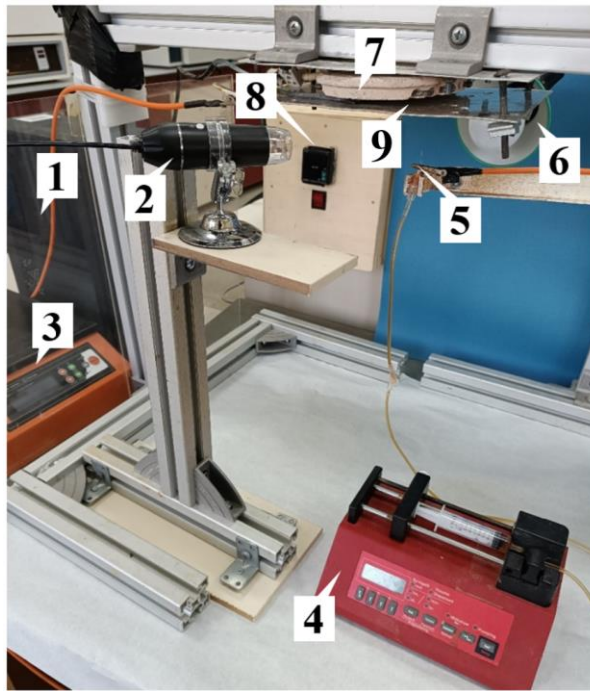


Figure 2.7. Particle Size Distribution Histogram

In the ESD method, the prepared ceramic pellet is placed in the space on the aluminum plate (7). The plate, on which pellets are placed, is screwed onto a metal shape containing a heating resistance (7). The heating process is controllable by a temperature controller (8). Thus, our pellet is positioned. The negative "-" end of the power supply (PlusElectronic 3000 High Voltage Supply, Turkey (3)) is connected to this plate. The prepared solution is drawn into the syringe. This syringe attaches to the syringe pump (New Era NE-1000) (4). For the syringe needle, a straight section tip is used instead of the traditional sharp needle which is used to establish vascular access (5). The positive "+" end of the power supply is connected to needle (5). By operating the syringe pump and power supply within the specified parameters, the solution coming to the syringe tip is separated from the needle tip with the help of the electrical field and moves upwards to the plate contrary to gravity. Here, the purpose of the solution is to reach the plate with the help of electrical difference. However, since the needle tip is positioned on the same vertical axis with the pellet in the empty space on the plate, some of these solutions also go on the ceramic pellet. A computer (1) and camera (2) are used to observe Taylor cone formation during coating. In order to better observation, it is preferable to have a dark background and a light source (6).

All components in the electrospray deposition setup are shown in the Figure 2.8. below.



1. PC
2. CCD Camera
3. High Voltage Power Supply
4. Syringe Pump
5. Needle
6. Light Source
7. Heater
8. Temperature Controller
9. GDC Pellet

Figure 2.8. ESD Setup

2.2. Statistical Experimental Design

ESD method contains quite a lot of parameters. These parameters can be sorted as applied potential difference, temperature, working distance, flow rate, evaporation temperature of solutions, surface tension, viscosity, coating time, post heat treatment, needle type, etc. There are currently studies in the literature on the effects of these parameters. Investigation of the effect of each parameter on the coating microstructure by examining parameters separately increases both the production costs and the spend time. Statistical experiment design method can be used in order to examine parameter effects more easily and to reduce production costs and spend time. In addition to reducing the number of experiments, we can understand which parameter is more effective with the Design of Experiments (DOE) methods. Above all, the use of resources will also be reduced. Box-Behnken Response Surface Design, a Plackett–Burman screening experimental design, full factorial design, etc. may be used as design of experiment method. The Plackett–Burman screening experimental design is selected to minimize the number of experiments, and to find out most important and effective parameters of experiments ^[66,79]. In this study, there were six continuous variables with low and high

levels of parameters as shown in Table 2.1 . These are the ranges in which the factor effects were covered.

Table 2.1. High and Low Levels of Selected Factors for Plackett-Burman screening design ^[66,79]

Factor no.	Factor effects	k	Low level	High level
1	Flow rate	A	0.01 ml/h	0.2 ml/h
2	Voltage	B	7 kV	20 kV
3	Working Distance	C	27 mm	50 mm
4	Concentration	D	0.004 M	0.01 M
5	Temperature	E	300 °C	350 °C
6	Duration	F	20 min	40 min

Table 2.2. Experimental design layout for Plackett–Burman approach ^[66,79]

No	Factor Effects						UFE (Unassigned Factor Effects)									
	A	B	C	D	E	F	G	H	J	K	L	M	N	O	P	
1	-	-	-	+	+	+	-	+	+	+	-	-	-	+	-	
2	+	-	-	-	-	+	+	+	-	-	-	-	+	+	+	
3	-	+	-	-	+	-	+	+	-	+	+	-	+	-	-	
4	+	+	-	+	-	-	-	+	+	-	+	-	-	-	+	
5	-	-	+	+	-	-	+	+	+	-	-	+	+	-	-	
6	+	-	+	-	+	-	-	+	-	+	-	+	-	-	+	
7	-	+	+	-	-	+	-	+	-	-	+	+	-	+	-	
8	+	+	+	+	+	+	+	+	+	+	+	+	+	+	+	
9	+	+	+	-	-	-	+	-	+	+	-	-	-	+	-	
10	-	+	+	+	+	-	-	-	-	-	-	-	+	+	+	
11	+	-	+	+	-	+	-	-	-	+	-	-	+	-	-	
12	-	-	+	-	+	+	+	-	+	-	+	-	-	-	+	
13	+	+	-	-	+	+	-	-	+	-	-	+	+	-	-	
14	-	+	-	+	-	+	+	-	-	+	-	+	-	-	+	
15	+	-	-	+	+	-	+	-	-	-	+	+	-	+	-	
16	-	-	-	-	-	-	-	-	+	+	+	+	+	+	+	

In order to calculate the main factor effects statistical calculations were done manually and are listed in Table 3.1 in the Title 3.1 following the method described in Harris and Lautenberger’s notes ^[79]. This procedure was also employed by Leigh et.al. ^[80] and Kavalcı et.al. ^[81]. To decide whether a factor is significant or not is determined

based on the critical minimum difference (MIN) value which can be calculated by Equation 2.1 and 2.2:

$$S_{FE} = \sqrt{\frac{1}{q}(UFE_1^2 + UFE_2^2 + \dots + UFE_q^2)} \quad (2.1)$$

$$[MIN] = t S_{FE} \quad (2.2)$$

where the number of unassigned factor effects are labelled with $q = n - p - 1$, $n =$ number of runs ($n = 16$ for 16 run Plackett-Burman design), $p =$ number of factors ($p = 6$ six factors were examined), $UFE =$ unassigned factor effects, $t = t_{dof, \alpha}$ (degrees of freedom (dof) = 9 because there were nine unassigned factor effects, $1 - \alpha =$ confidence coefficient). UFE are a mixture of two factor interactions a list of which is available in [79].

2.3. Experimental Method

The experimental method was shown schematically in Figure 2.9. PVA binder which is 2% of the GDC powder weight, was dissolved at enough amount of pure water. It was mixed with commercial GDC powder. After applying hot air to remove water, powder was crushed and mixed in agate mortar.

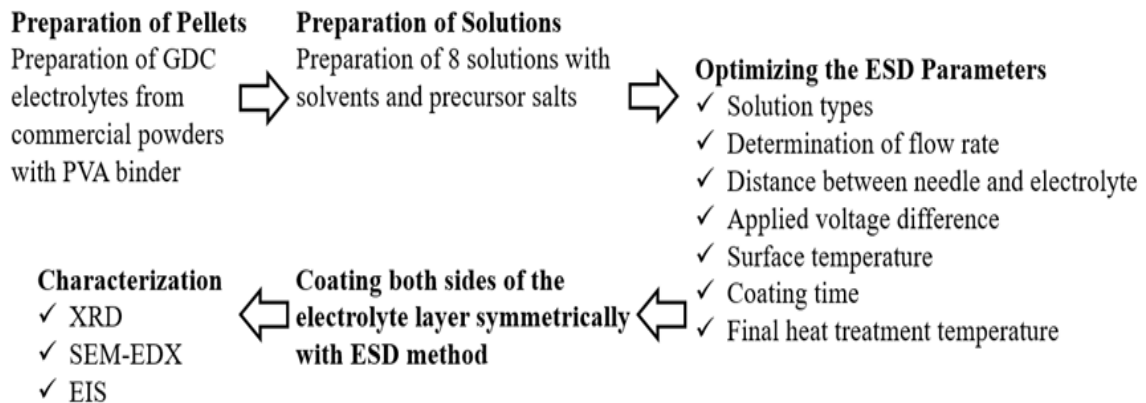


Figure 2.9. Schematic of Experimental Method

Prepared GDC powder with PVA binder was pressed in a hydraulic press. Pressing process is done with 2 steps. First step includes pressing for deairing process of powder and pressure was relased after reaching 2 metric tones. Second step includes pressing to 6 metric tones. Then, pellets were pressed and ready for sintering process. The pellets were sintered in a box kiln at 1400 °C for 8 hours shown graphically in Figure 2.10.

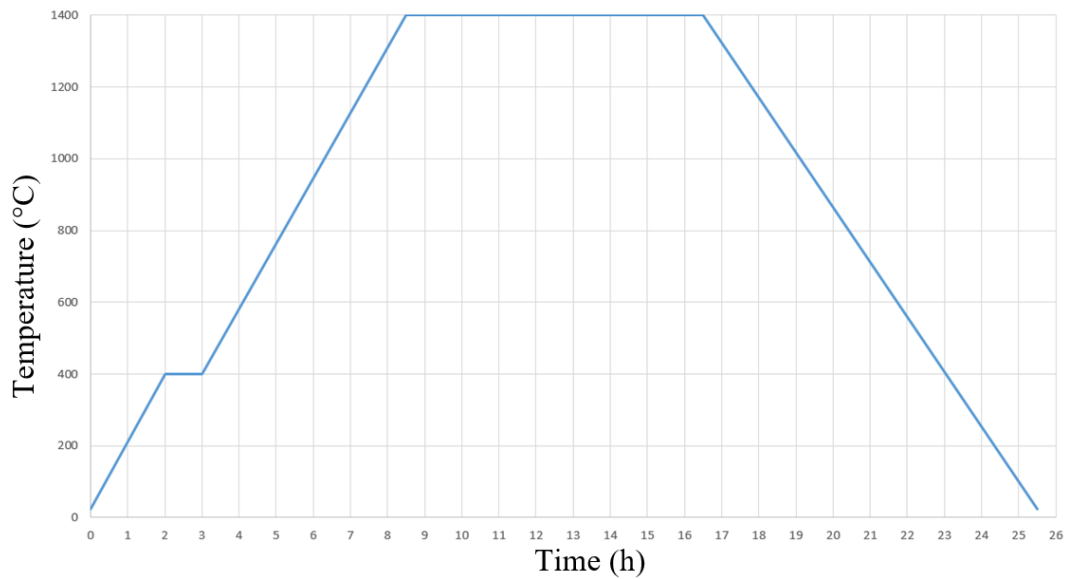


Figure 2.10. Temperature vs Time Graph of Sintering Process

The SEM image taken on the GDC pellet cross-section is shown in Figure 2.11. XRD analysis result after the sintering process of pressed GDC pellet from powder is shown in Figure 2.12.

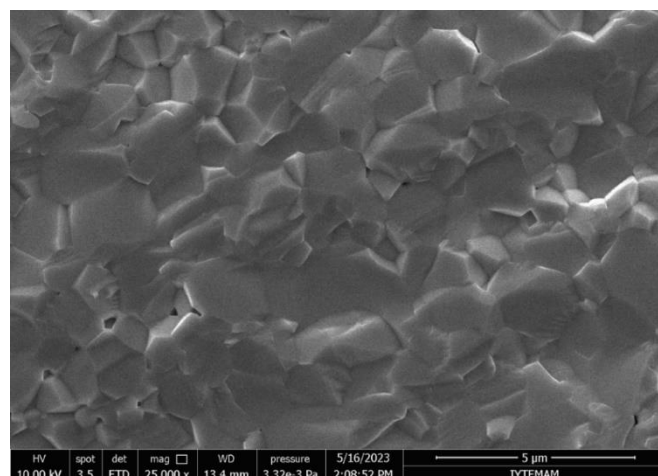


Figure 2.11. SEM Image of Dense GDC Ceramic Pellet After Sintering Process

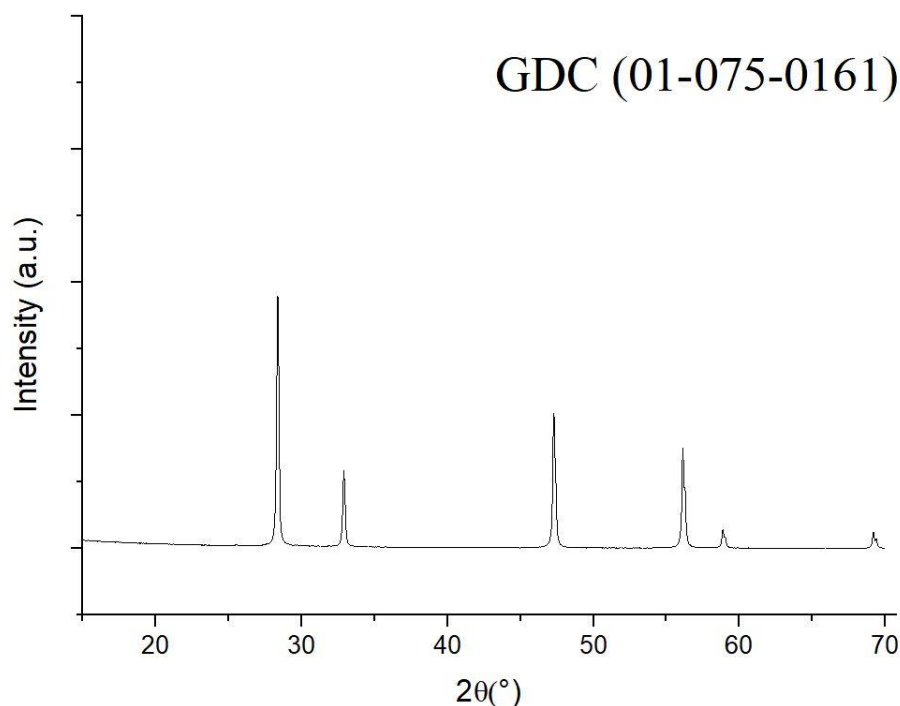


Figure 2.12. XRD Peaks of GDC Pellet

Cathode layer compositions in different combinations were prepared shown in Table 2.3, 2.4 and 2.5. $\text{La}(\text{NO}_3)_3 \cdot 6\text{H}_2\text{O}$ (Alfa-Aesar >%99), $\text{SrCl}_2 \cdot 6\text{H}_2\text{O}$ (Alfa-Aesar >%99), $\text{Ca}(\text{NO}_3)_2 \cdot 4\text{H}_2\text{O}$ (Merck, 1.02121.0500), $\text{Fe}(\text{NO}_3)_3 \cdot 9\text{H}_2\text{O}$ (Alfa-Aesar >%98), $\text{Cr}(\text{NO}_3)_3 \cdot 9\text{H}_2\text{O}$ (Alfa-Aesar >%98.5), $\text{Ce}(\text{NO}_3)_3 \cdot 6\text{H}_2\text{O}$ (Sigma Aldrich, 238538), $\text{Gd}(\text{NO}_3)_3 \cdot 6\text{H}_2\text{O}$ (Sigma Aldrich, 211591) salts were used.

On the optimization of ESD parameters part of the thesis, experiments were designed with using Plackett-Burmann experimental design approach which aimed to decrease number of experiments. Concentration of solution is also a design parameter like working distance, flow rate, etc. On this part, solutions were prepared in 0.01M as high level and 0.004 M as low level. Weighed salts for intended molarity were mixed with pure water and ethylene glycol in magnetic stirrer with 250 rpm at 80 °C. Vaporization the pure water in solution and water in the salts was the expected at this step. After vaporization process, 2-Butoxyethanol was added to reduce surface tension and to improve the properties of the polymeric precursor. Solution was prepared with final stirring process nearly 30 minutes. Solution preparation on the optimization of ESD parameters part of thesis is also same as solution preparation at effects of solution changing part of thesis with 2nd Type Solvents.

On the effects of solution changing part of the thesis, solutions were prepared in 0.004 M because sample 16 had the best coating structure with 0.004 M in the first part of the thesis. Salts in solution A to D were mixed in 1st type of solvents in magnetic stirrer at room temperature for 1 hour. In these solvents, there is an ethanol / butyl carbitol volume ratio as 1:2.

The solutions prepared with different solvent and salt mixtures were sprayed on the pellet with the help of a needle, syringe pump, power supply and coating process was done by ESD method.

Scanning Electron Microscope (SEM, Philips XL 30S FEG) were used for Microstructural and compositional analyzes. Energy dispersive spectroscopy (EDX) was used for elemental analysis. Crystal structures were examined by x-ray diffraction (XRD, Panalytical X-Pert Pro). Cu K α radiation was chosen as the X-ray source. Electrochemical performances of the coated electrodes were evaluated by electrochemical impedance spectroscopy (EIS). Analyzes were performed on symmetric half cells in Coating/GDC/Coating configuration. Ag paste was applied to the electrode surfaces for accomplished connection and Ag wires were adhered to the Ag paste surface by applying high temperature ceramic adhesive Ceramabond. Measurements were made in air at 500-700 °C using the BioLogic SP-150 potentiostat/galvanostat/EIS analyzer. The scanned frequency range is 10⁻¹ - 10⁴ Hz, the excitation voltage is ± 10 mV.

Table 2.3. Solvent Types

1 st Type Solvents	2 nd Type Solvents
Ethanol	Ethylene glycol
Butyl Carbitol	2-Butoxyethanol

Table 2.4. Precursor Salts

Precursor Salts		
$\text{La}_{0.30}\text{Sr}_{0.70}\text{Fe}_{0.70}\text{Cr}_{0.30}\text{O}_{3-\delta}$	$\text{La}_{0.30}\text{Ca}_{0.70}\text{Fe}_{0.70}\text{Cr}_{0.30}\text{O}_{3-\delta}$	$\text{Ce}_{0.9}\text{Gd}_{0.1}\text{O}_{1.95}$ (GDC)
L: $\text{La}(\text{NO}_3)_3 \cdot 6\text{H}_2\text{O}$	L: $\text{La}(\text{NO}_3)_3 \cdot 6\text{H}_2\text{O}$	$\text{Ce}(\text{NO}_3)_3 \cdot 6\text{H}_2\text{O}$
S: $\text{SrCl}_2 \cdot 6\text{H}_2\text{O}$	C: $\text{Ca}(\text{NO}_3)_2 \cdot 4\text{H}_2\text{O}$	
F: $\text{Fe}(\text{NO}_3)_3 \cdot 9\text{H}_2\text{O}$	F: $\text{Fe}(\text{NO}_3)_3 \cdot 9\text{H}_2\text{O}$	$\text{Gd}(\text{NO}_3)_3 \cdot 6\text{H}_2\text{O}$
Cr: $\text{Cr}(\text{NO}_3)_3 \cdot 9\text{H}_2\text{O}$	Cr: $\text{Cr}(\text{NO}_3)_3 \cdot 9\text{H}_2\text{O}$	

Table 2.5. Content of Solutions

Solution Name	Solvent Type	Precursor Salts
A	1 st	LSFCr
B	1 st	LSFCr + GDC
C	1 st	LCFCr
D	1 st	LCFCr + GDC
E	2 nd	LSFCr
F	2 nd	LSFCr + GDC
G	2 nd	LCFCr
H	2 nd	LCFCr + GDC

CHAPTER 3

RESULTS

3.1. Scoring of the Coatings

SEM images were taken on the coatings made according to the experimental design plan. In the images obtained, it was determined that some coatings had a dense cathode coating, some coatings could not adhere to the electrolyte, and some coatings had the desired reticular (coral-like) structure. The scores between 1 and 5 were given to the coatings according to whether or not the intended coral-like structure was achieved. Example scores and their reasons are given below. Table 3.1 was created by arranging the low and high levels specified in the Table 2.1 with the layout specified in Table 2.2 and coating quality results as scores from 1 to 5. The scores here represent the coating quality which means the success of obtaining the desired reticular structure in the thesis.

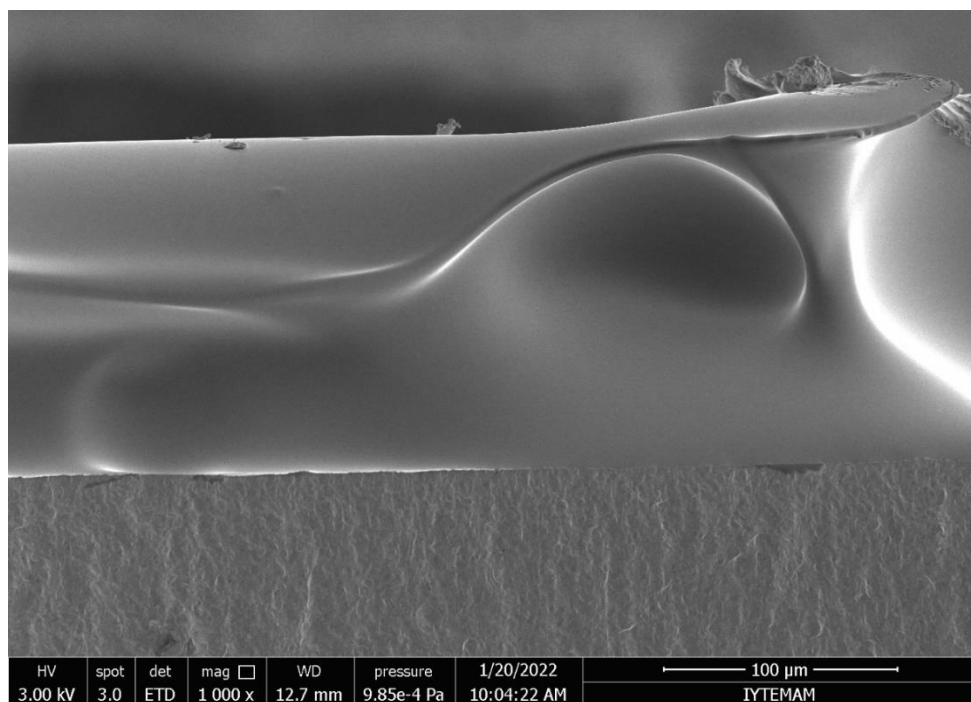


Figure 3.1. Example of Score 1 with Experiment 15

There can be some isolated pockets of pores. However, the coating structure may be dense. Experiment 14 can be given as an example of this situation.

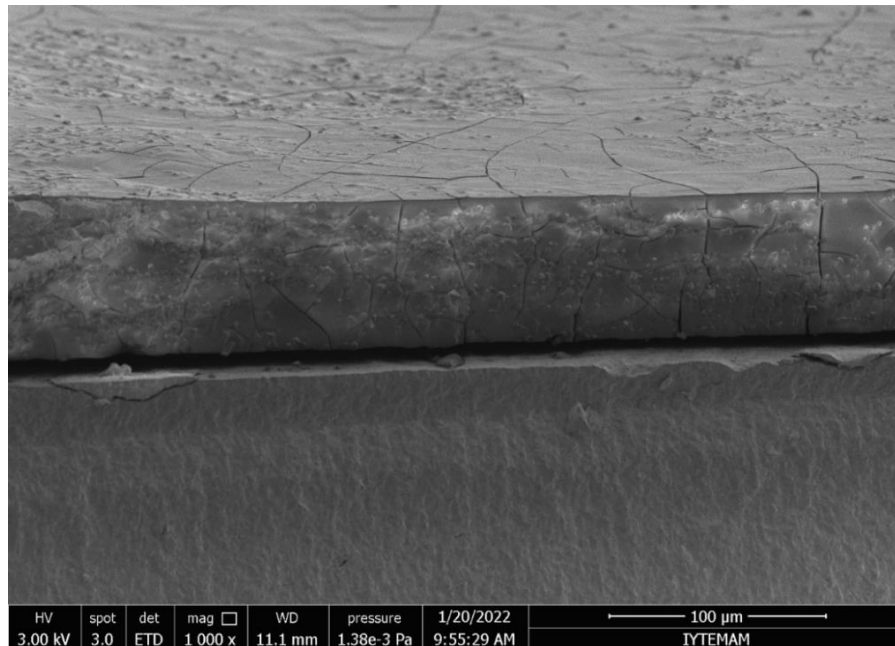


Figure 3.2. Example of Score 2 with Experiment 14

The dense structure can decrease with the increasing of voids. But the structure has marginal reticular structures. Experiment 11 can be given as an example of this scoring.

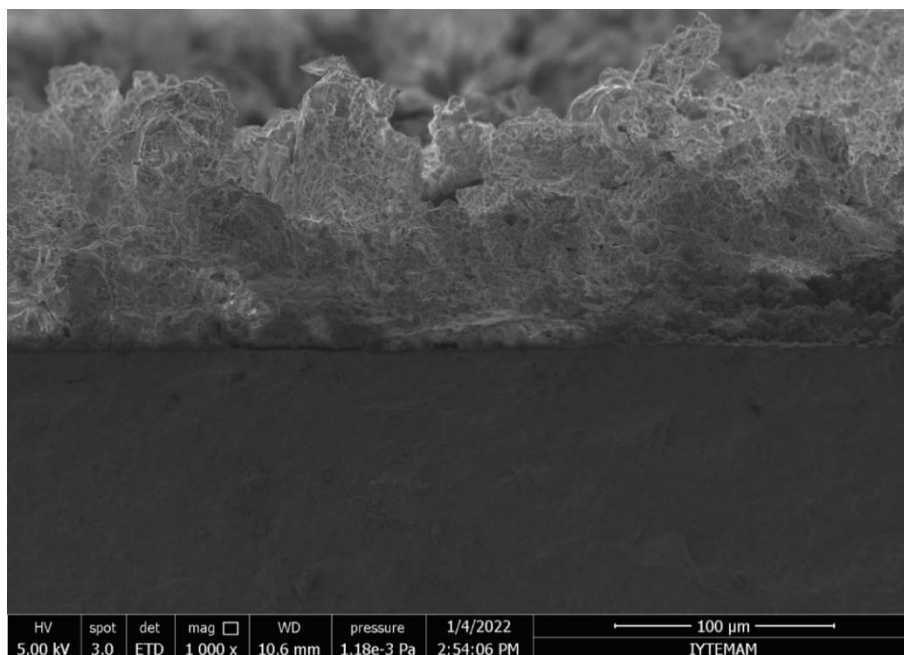


Figure 3.3. Example of Score 3 with Experiment 11

The coating is expected to be composed entirely of reticular structures. Score was given to structures that mostly consisted of reticular structures but were not at the desired level. Experiment 4 can be given as an example of these structures.

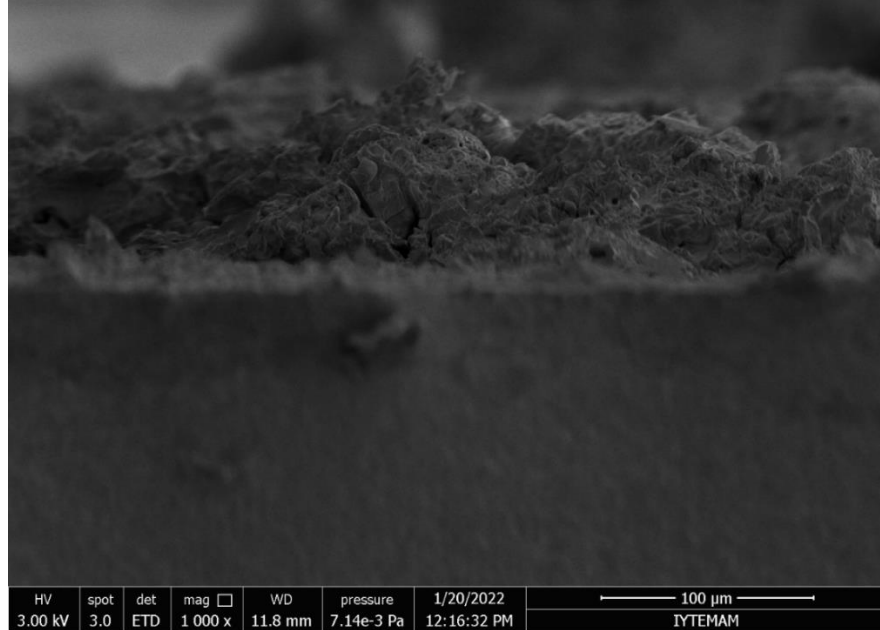


Figure 3.4. Example of Score 4 with Experiment 4

There are structures in which the expected reticular structure is completely formed. Experiment 3 can be given as an example of these structures.

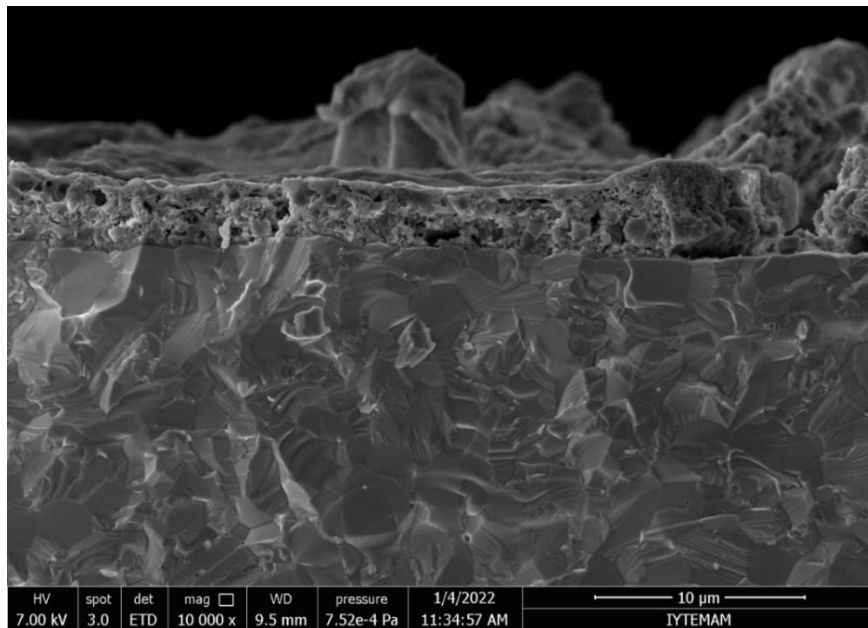


Figure 3.5. Example of Score 5 with Experiment 3

Table 3.1. Experiments designed via Plackett–Burman approach [66,79]

Experiment No	A (Flow rate)	B (Voltage)	C (Working Distance)	D (Concentration)	E (Temperature)	F (Duration)	Response (Output)
1	0.01	7	27	0.010	350	40	2
2	0.20	7	27	0.004	300	40	5
3	0.01	20	27	0.004	350	20	5
4	0.20	20	27	0.010	300	20	2
5	0.01	7	50	0.010	300	20	4
6	0.20	7	50	0.004	350	20	3
7	0.01	20	50	0.004	300	40	5
8	0.20	20	50	0.010	350	40	1
9	0.20	20	50	0.004	300	20	2
10	0.01	20	50	0.010	350	20	5
11	0.20	7	50	0.010	300	40	3
12	0.01	7	50	0.004	350	40	1
13	0.20	20	27	0.004	350	40	2
14	0.01	20	27	0.010	300	40	3
15	0.20	7	27	0.010	350	20	1
16	0.01	7	27	0.004	300	20	5*

*The best coating structure as determined by qualitative assessment.

3.2. Significant Parameters w.r.t. Plackett-Burman Design

The manually calculated MIN values with using Equation 2.1 and 2.2 is shown in Table 3.2. Critical minimum difference (MIN) value is the limit to show the parameters are significant or not. MIN value can be calculated for different confidence levels with using Equation 2.2 in (Title 2.3) . As a result, Flow rate has a greater absolute effect value than calculated MIN value at 90% confidence level. On the other hand, it has a smaller absolute effect value than calculated MIN value at 95% confidence level. In this situation, flow rate is the most significant factor among all parameters by providing the 90% confidence level. Flow rate and temperature parameters are both significant factors at 80% confidence level as well because their absolute effect values are higher than calculated MIN value. Additional ladder design experiments are done to prove the effect of the flow rate.

3.3. Chemical Analysis of Precipitates Obtained by Evaporation of the Solutions

Solutions which are prepared by stoichiometric proportions, are tested with electron dispersive spectroscopy (EDX) analysis. Results show that there were some errors on stoichiometry of solutions. As a result, weighing of salts and solvents with precision scales had to be done carefully. By taking errors into consideration, final stoichiometric proportions were corrected and solutions were prepared for experiments. Calculations were made by taking the average of the measurements taken from 3 different regions during the EDX analysis. Table 3.3, 3.4, 3.5 and 3.6 were shown below with solution name, number of spectrum, weight and atomic percentage values of elements in the solutions.

Table 3.3. EDX Results of Solutions A and E

Solution	Spectrum	Wt %				Atomic %			
		La	Sr	Fe	Cr	La	Sr	Fe	Cr
A	1	18.2	64.4	11.6	5.8	11.1	62.1	17.5	9.3
	2	32.6	27.1	27.8	12.6	18.3	24.1	38.8	18.8
	3	23.2	54.7	15.3	6.8	13.9	52.2	22.9	11.0
	Average	24.6	48.7	18.2	8.4	14.4	46.1	26.4	13.0
E	1	24.5	33.8	29.7	12.0	13.3	29.1	40.1	17.5
	2	18.7	25.8	39.0	16.5	9.3	20.4	48.3	22.0
	3	23.2	35.5	28.7	12.6	12.6	30.5	38.7	18.3
	Average	22.2	31.7	32.4	13.7	11.7	26.7	42.4	19.3

Table 3.4. EDX Results of Solutions C and G

Solution	Spectrum	Wt %				Atomic %			
		La	Ca	Fe	Cr	La	Ca	Fe	Cr
C	1	37.1	22.0	28.5	12.5	17.9	44.2	10.3	27.6
	2	36.1	21.9	29.0	13.1	17.7	44.9	10.3	27.5
	3	35.6	22.4	28.7	13.3	17.1	45.3	10.3	27.3
	Average	36.2	22.1	28.7	13.0	17.6	44.8	10.3	27.5
G	1	22.1	15.3	44.3	18.3	9.4	22.7	47.0	20.9
	2	30.9	26.4	30.0	12.8	13.4	39.6	32.3	14.9
	3	27.5	21.5	35.9	15.2	11.9	32.2	38.5	17.5
	Average	26.8	21.1	36.7	15.4	11.5	31.5	39.2	17.7

Table 3.5. EDX Results of Solutions B and F

Solution	Spectrum	Wt %						Atomic %					
		La	Sr	Fe	Cr	Gd	Ce	La	Sr	Fe	Cr	Gd	Ce
B	1	17.6	24.4	14.9	5.8	4.4	33.0	12.7	4.9	31.1	13.9	4.2	33.2
	2	18.2	23.8	14.2	5.7	4.5	33.6	11.9	20.8	23.6	12.0	3.5	28.2
	3	16.3	25.1	14.1	5.3	4.9	31.7	12.0	21.6	22.3	12.0	3.6	28.5
Average		17.3	24.4	14.4	5.6	4.6	32.8	12.2	15.8	25.7	12.6	3.8	29.9
F	1	11.9	16.9	18.1	7.1	5.1	41.0	8.0	18.2	30.5	12.7	5.1	27.5
	2	11.5	17.3	16.4	6.2	5.5	43.2	7.9	19.1	28.3	11.5	3.3	29.7
	3	11.5	17.1	17.1	6.9	5.3	42.2	7.7	17.9	31.3	14.9	4.1	36.2
Average		11.6	17.1	17.2	6.7	5.3	42.1	7.9	18.4	30.1	13.1	4.2	31.2

Table 3.6. EDX Results of Solutions D and H

Solution	Spectrum	Wt %						Atomic %					
		La	Ca	Fe	Cr	Gd	Ce	La	Ca	Fe	Cr	Gd	Ce
D	1	20.2	12.8	16.8	7.5	4.6	38.1	11.3	33.2	7.9	24.6	1.8	21.2
	2	20.7	13.1	16.6	7.0	4.8	37.8	12.1	35.7	6.7	22.2	1.7	21.7
	3	20.0	12.9	16.8	7.0	5.3	38.2	10.9	31.7	7.9	25.5	2.5	21.5
Average		20.3	12.9	16.7	7.2	4.9	38.0	11.4	33.5	7.5	24.1	2.0	21.5
H	1	19.1	12.6	14.7	6.7	6.4	40.6	11.7	12.6	14.7	6.7	3.5	24.7
	2	20.6	10.9	15.1	7.2	5.4	40.8	12.9	23.5	23.5	12.0	3.0	25.2
	3	20.3	11.0	15.0	6.2	5.9	41.7	12.8	24.1	23.5	10.4	3.3	26.0
Average		20.0	11.5	14.9	6.7	5.9	41.0	12.4	20.1	20.6	9.7	3.2	25.3

According to the obtained EDX results, stoichiometric proportions were calculated for each solution shown in Table 3.7 by using Atomic % values. Stoichiometric shifts were observed according to the values found. Since this situation was determined in the late period of the thesis, it could not be intervened.

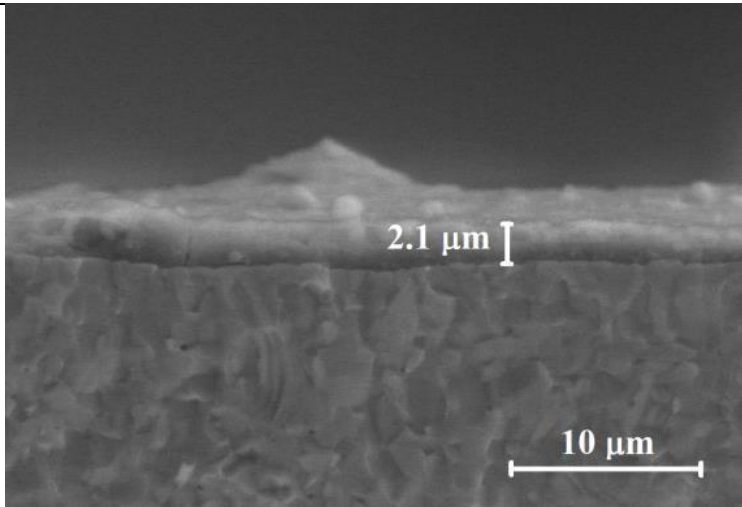
Table 3.7. Calculated Stoichiometric Proportions of Solutions

Solution Name	Stoichiometric Proportions
A	La _{0.16} Sr _{0.84} Fe _{0.65} Cr _{0.35}
B	La _{0.33} Sr _{0.67} Fe _{0.65} Cr _{0.35} Gd _{0.10} Ce _{0.90}
C	La _{0.10} Ca _{0.90} Fe _{0.26} Cr _{0.74}
D	La _{0.09} Ca _{0.91} Fe _{0.22} Cr _{0.78} Gd _{0.08} Ce _{0.92}
E	La _{0.22} Sr _{0.78} Fe _{0.67} Cr _{0.33}
F	La _{0.21} Sr _{0.79} Fe _{0.68} Cr _{0.32} Gd _{0.11} Ce _{0.89}
G	La _{0.10} Ca _{0.90} Fe _{0.67} Cr _{0.33}
H	La _{0.15} Ca _{0.85} Fe _{0.66} Cr _{0.34} Gd _{0.10} Ce _{0.90}

3.4. Ladder Design Experiments for the Effect of Flow Rate

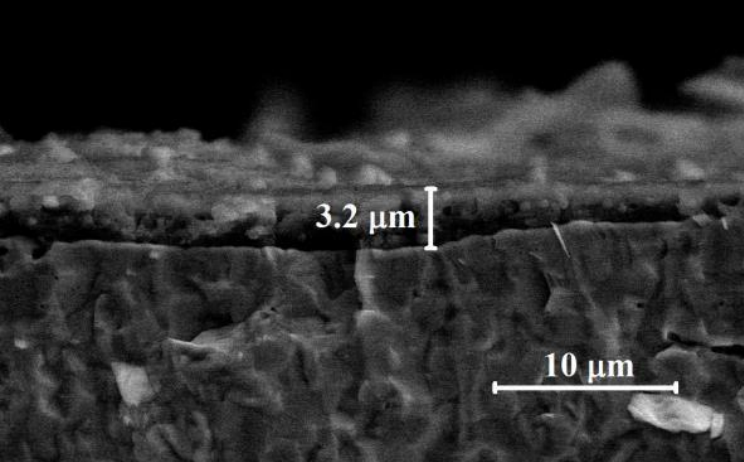
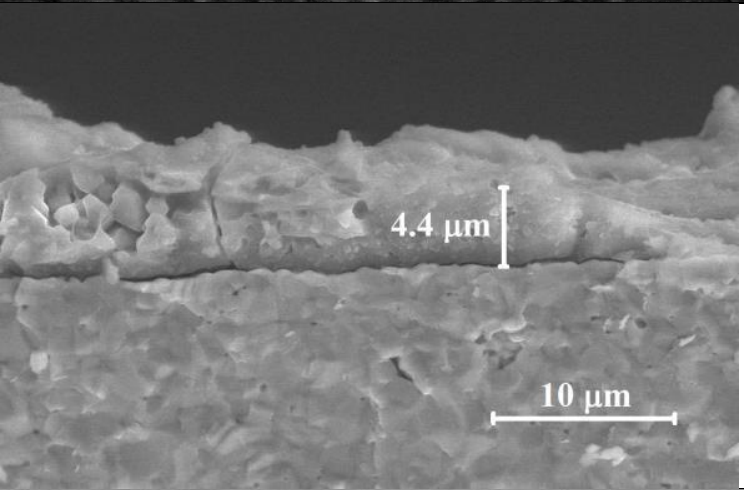
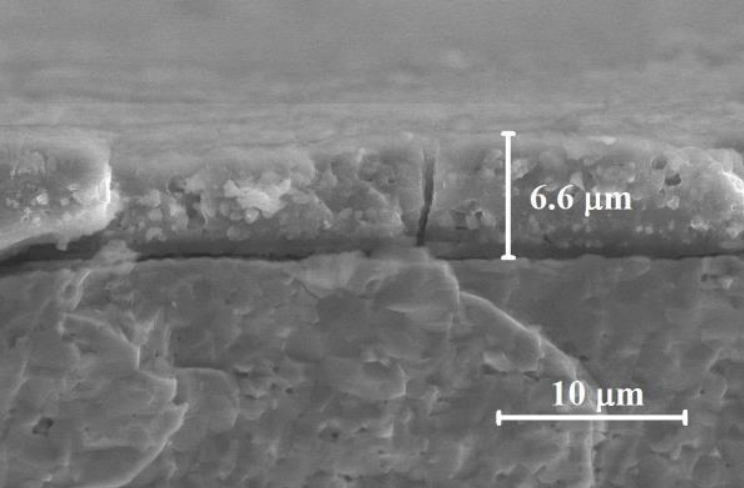
Sample number 16 has best reticular structure according to scoring all coating structures. The flow rate is the most important factor in the calculations made according to the Plackett-Burman experimental design. Accordingly, 3 more experiments which called 16a, 16b and 16c, were carried out by changing only the flow rate among the experimental parameters of Experiment 16. It was observed that the coating thickness changed in direct proportion with the flow rate. SEM images obtained from these experiments are shown in Table 3.8.

Table 3.8. Flow Rate Difference in SEM Images

Exp No	Flow Rate	SEM Images
16a	0.005	

(cont. on next page)

Table 3.8. (cont.).

16	0.010	
16b	0.015	
16c	0.020	

3.5. Coating Structure as Observed from Top view

Up to now, the images were taken perpendicular to the cross-sectional area after the GDC pellets were broken. In this section, the images were taken from the top view of the coating on the pellet. Like the coating structure, the coating distribution also varies with the parameters. The homogeneity of the coating and its adhesion to the surface are among the factors affecting the success of the coating process. If a coating is made without a Taylor cone, clumping may appear on the pellet. Taylor cone ensures homogeneous distribution of the solution to form a coating. As a matter of fact, thick and clumped coatings may be plucked from the pellet while the pellets are broken to get a cross-sectional view. In terms of the precision of the measurements, it is desirable that the coating thickness are equal in every region. Examples of SEM images taken perpendicular to coating on pellets which have homogeneous and non-homogeneous coating distribution are shown below.

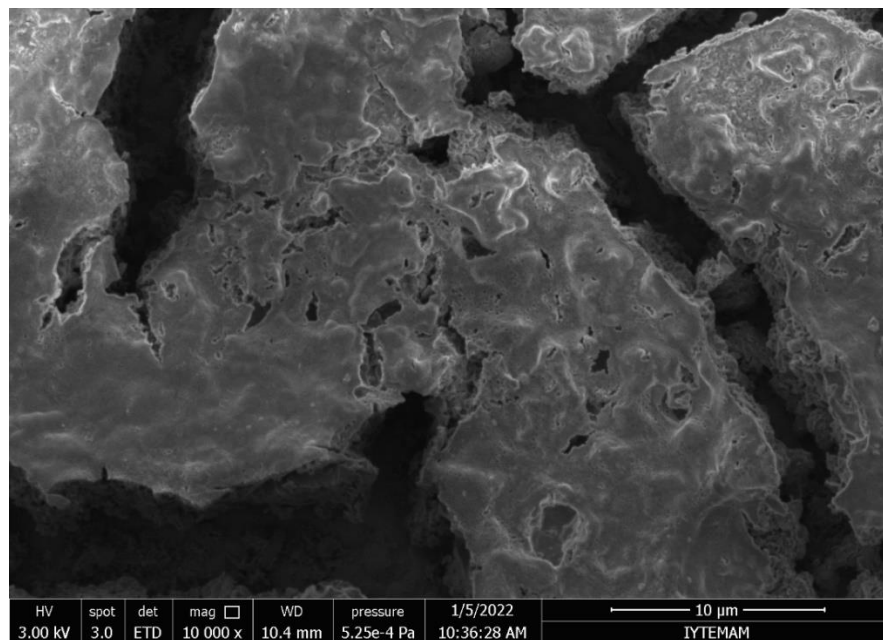


Figure 3.6. SEM Image of Homogeneous Coating Distribution on Experiment 3

Specific to Experiment 3 as given example, the reticular structure, which was handled and scored as successful (5 points), is visible even in the top view SEM image.

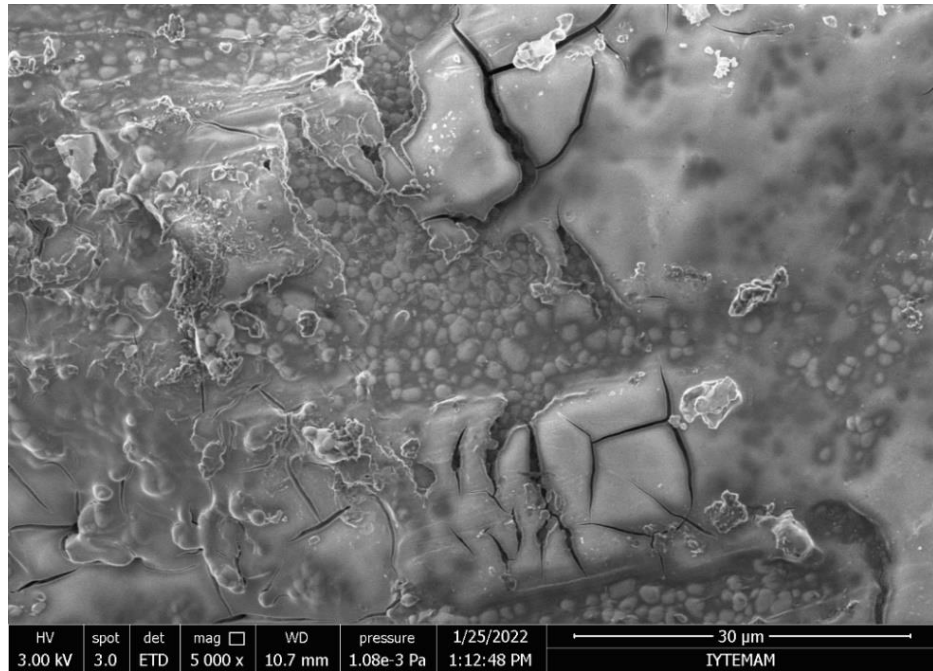


Figure 3.7. SEM Image of Non-homogeneous Coating Distribution on Experiment 15

The coating made with solution A and B are homogeneously distributed over the entire surface as seen in the Figure 3.8 and 3.9. The obvious point for these coatings is that the coating is glassy. There are crystal particles on the coatings. These crystals, originating from the salts present in solution, are clearly visible on SEM images. EDX analyzes of these particles were also made and are available in other titles.

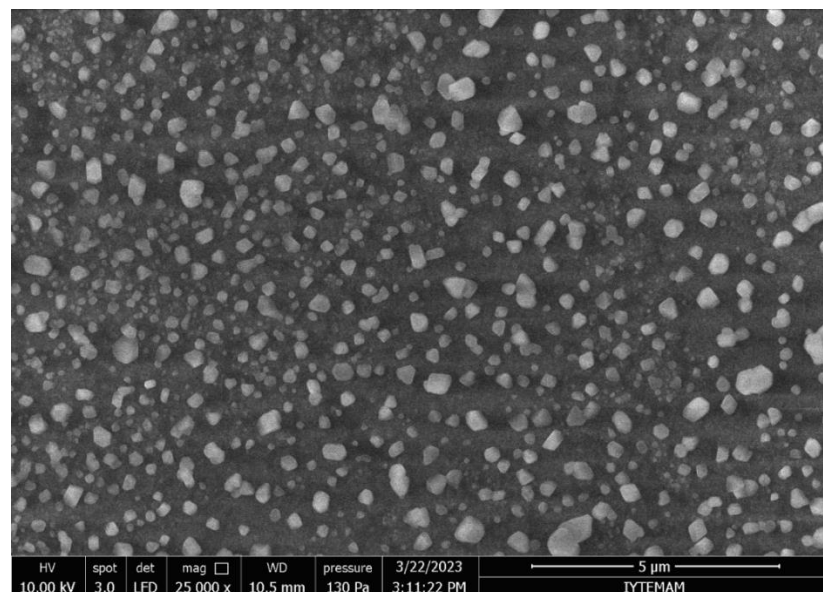


Figure 3.8. SEM Image of Coated GDC Pellet by Solution A

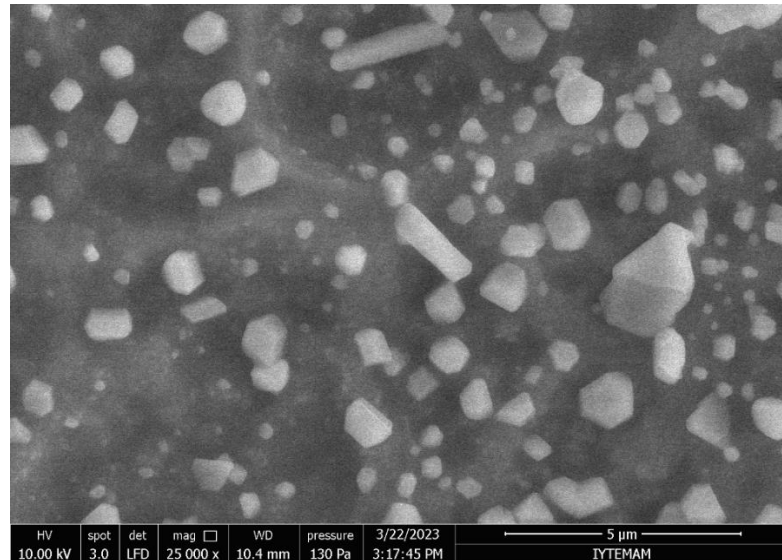


Figure 3.9. SEM Image of Coated GDC Pellet by Solution B

Particles seen in coatings made with solutions A and B were not seen in coatings with solutions C and D. The only difference at this point is the Sr and Ca salts used in the solutions. While the presence of crystal particles on the surface was in solutions containing Sr, no particles were observed in coatings made with solutions containing Ca. Glassy coatings were observed also by these solutions.

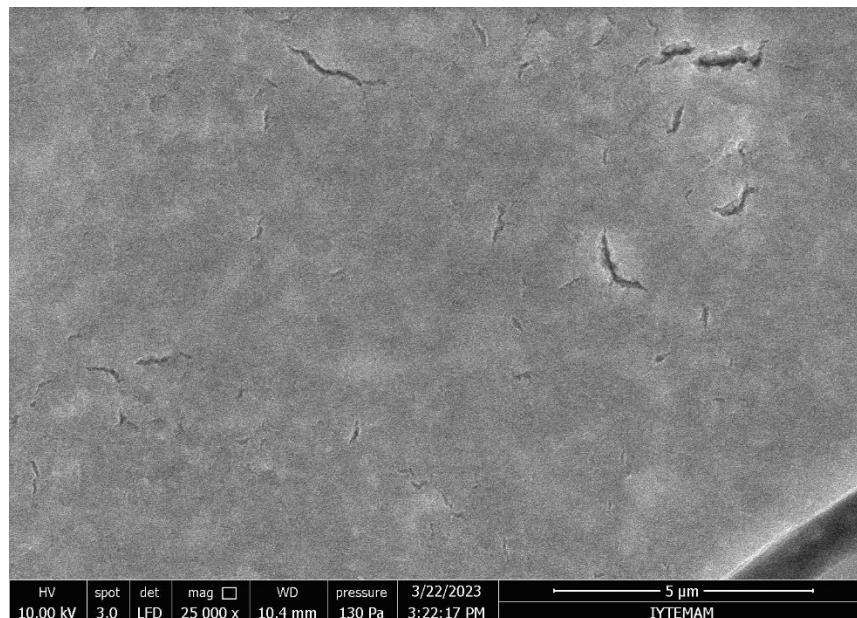


Figure 3.10. SEM Image of Coated GDC Pellet by Solution C

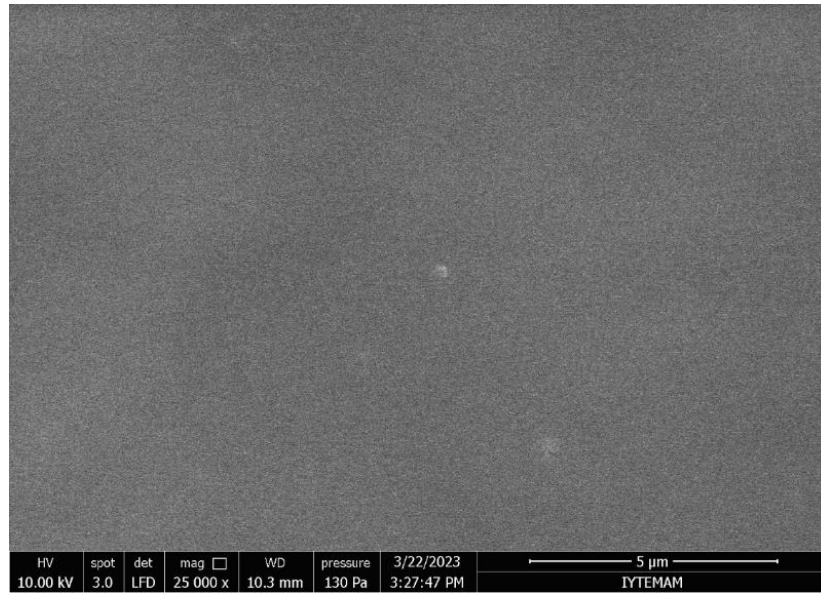


Figure 3.11. SEM Image of Coated GDC Pellet by Solution D

In the coatings made with the E solution, which was evaluated in the first part of the thesis, and the F solution prepared in this part, the reticular structure was observed even on SEM image from top view.

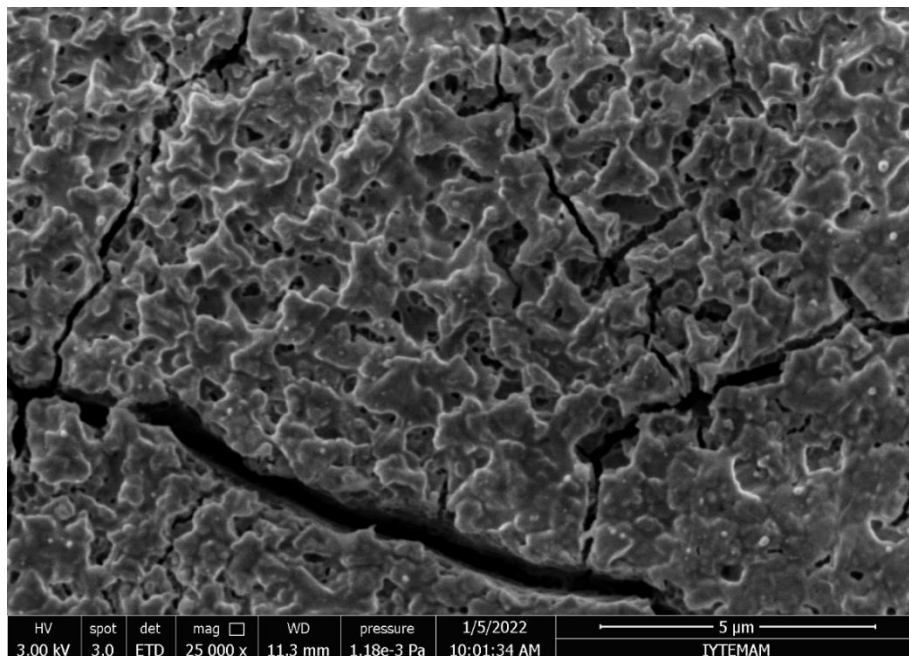


Figure 3.12. SEM Image of Coated GDC Pellet by Solution E

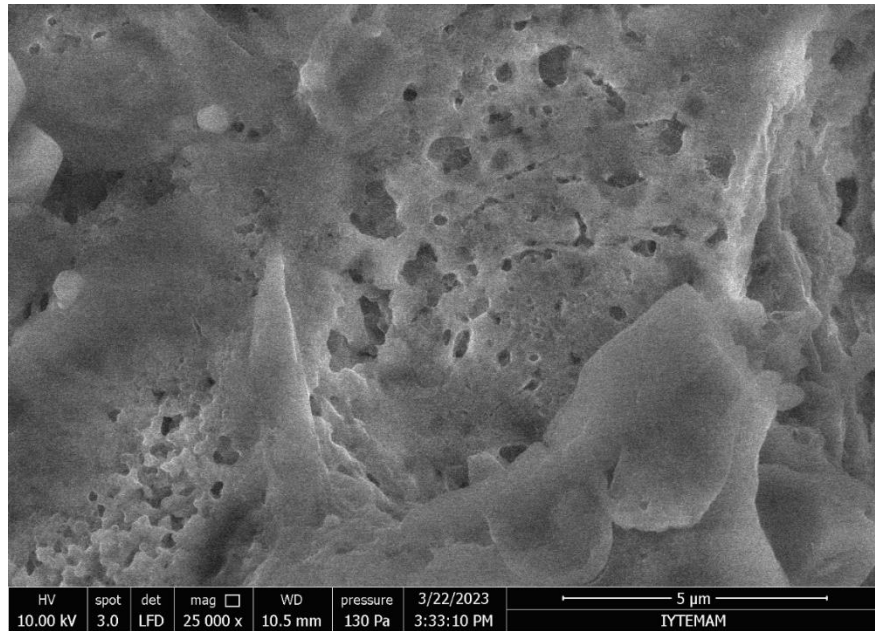


Figure 3.13. SEM Image of Coated GDC Pellet by Solution F

The first striking point in the SEM images of the coatings made with G and H solutions is the presence of distinct and deep cracks on the surface of coatings.

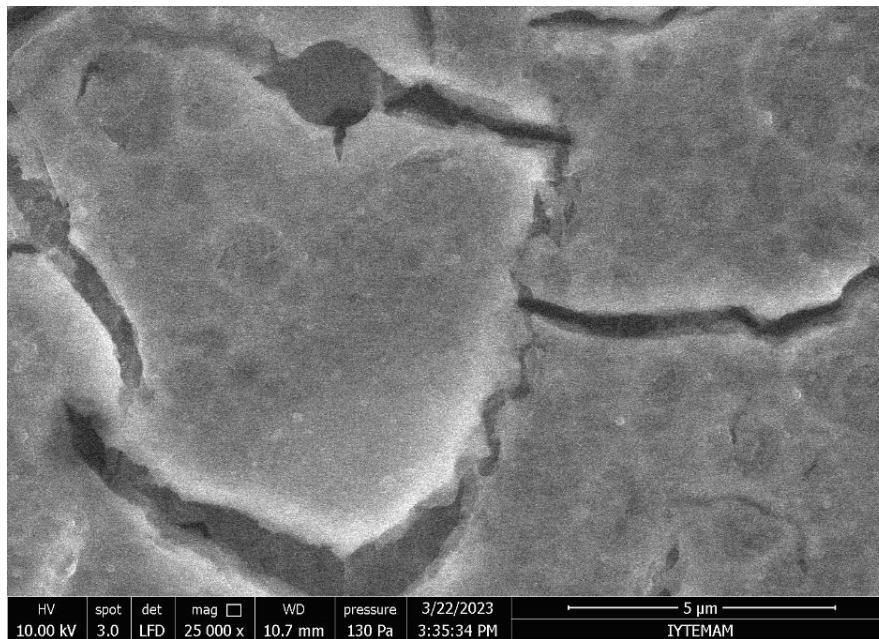


Figure 3.14. SEM Image of Coated GDC Pellet by Solution G

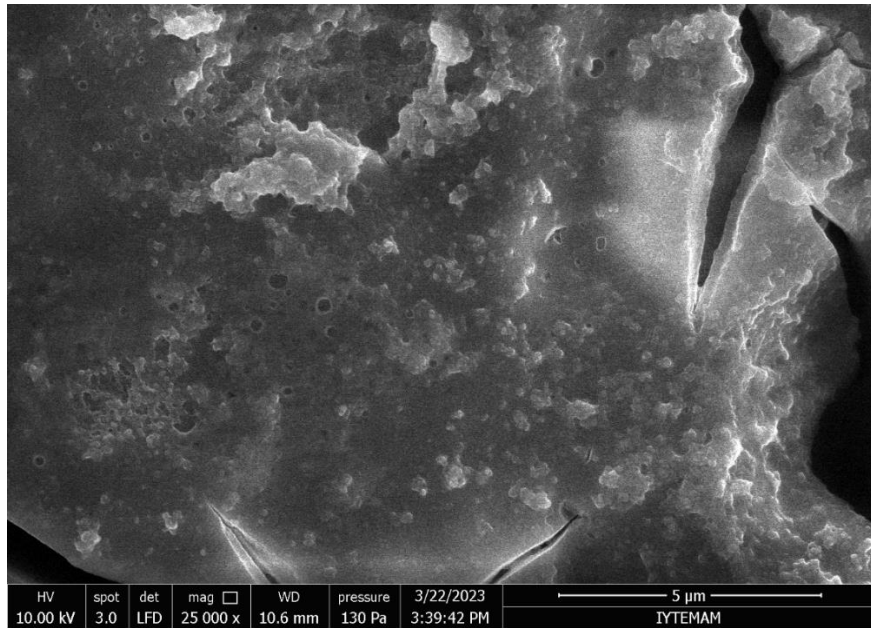


Figure 3.15. SEM Image of Coated GDC Pellet by Solution H

Glassy structures were observed in the SEM images taken from the coated pellets with solutions prepared using the 1st type of solvents. In addition, it was observed that white particles were placed on the coating surface in pellets that were coated with solutions A and B. It was stated that the Sr salt may not have been completely dissolved in the solution because EDX analysis results show these particles contain high percentages of Sr. It was also observed that coatings made with solutions prepared with 2nd type solvents were thick, containing voids (non-glassy), cracked, etc.

3.6. Average Thickness of Coatings

The coated pellets were broken to see the cross-section of coating and SEM images were taken. Coating thicknesses were measured on cross-sectional SEM images. The following Table 3.8 was created by taking the average of the values taken from different points. Reasons such as the breaking point, the proper separation of the coating, and the SEM images from different areas may cause errors. According to the Table 3.9, it was seen that the thickness of the coatings in which the desired reticular structure was formed was higher than the others. In the literature, Marinha et al ^[39] studied that the coating of $\text{La}_{0.6}\text{Sr}_{0.4}\text{Co}_{0.2}\text{Fe}_{0.8}\text{O}_{3-d}$ on GDC by ESD method using 1.5 ml/h flow rate, 15

mm working distance, 300 °C substrate temperature, 1 h coating time. The coating thickness of their sample is nearly 4 μm .

Table 3.9. Average Thickness of Coatings on Second Part Experiments

Solution Type	Average Thickness of Coating
A	2.5 μm
B	1.2 μm
C	1.3 μm
D	1.0 μm
E	2.9 μm
F	5.1 μm
G	1.9 μm
H	1.3 μm

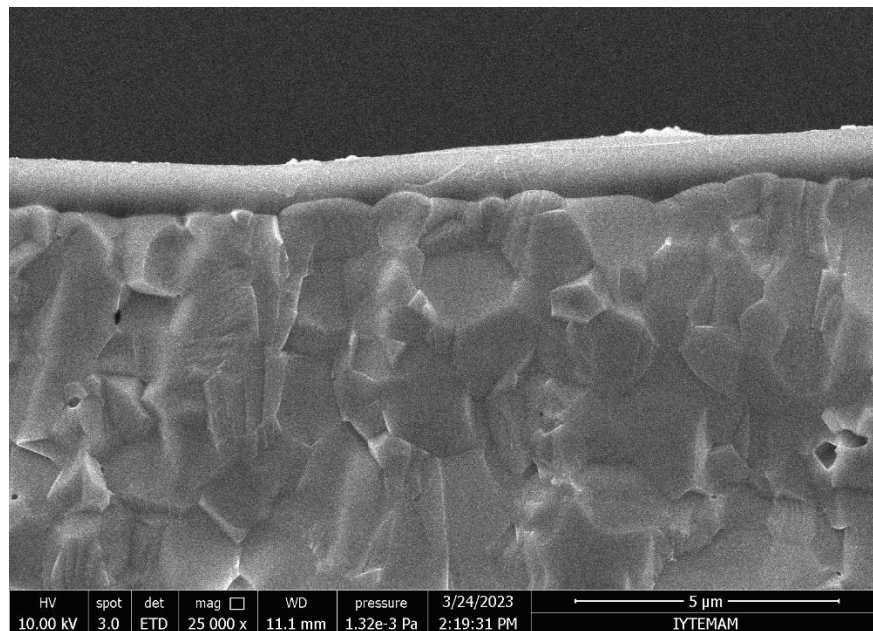


Figure 3.16. Cross-sectional SEM Image of Coated GDC Pellet by Solution D

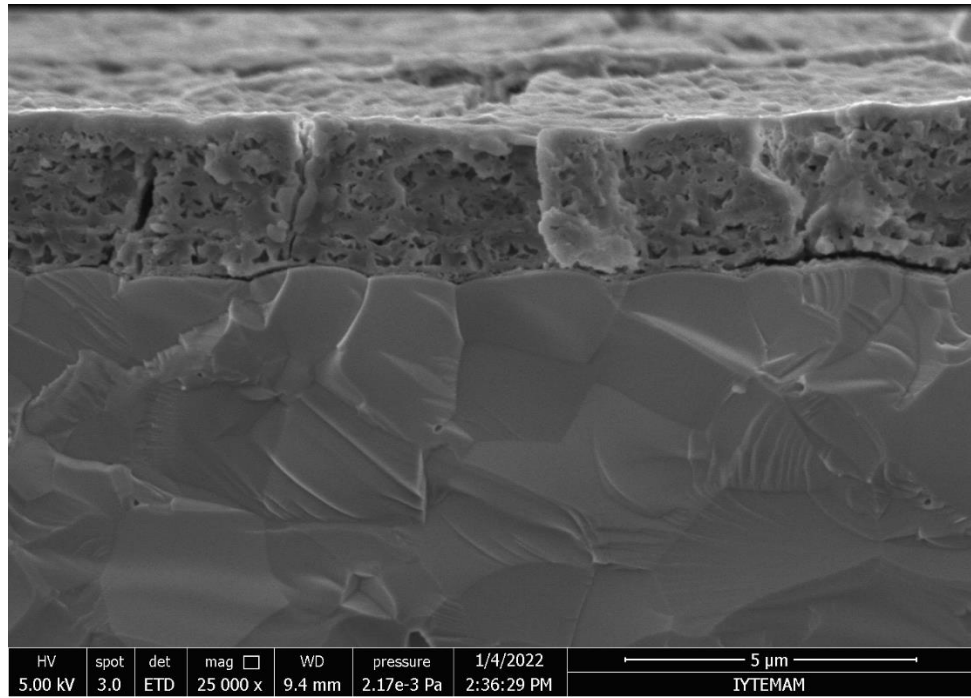


Figure 3.17. Cross-sectional SEM Image of Coated GDC Pellet by Solution E

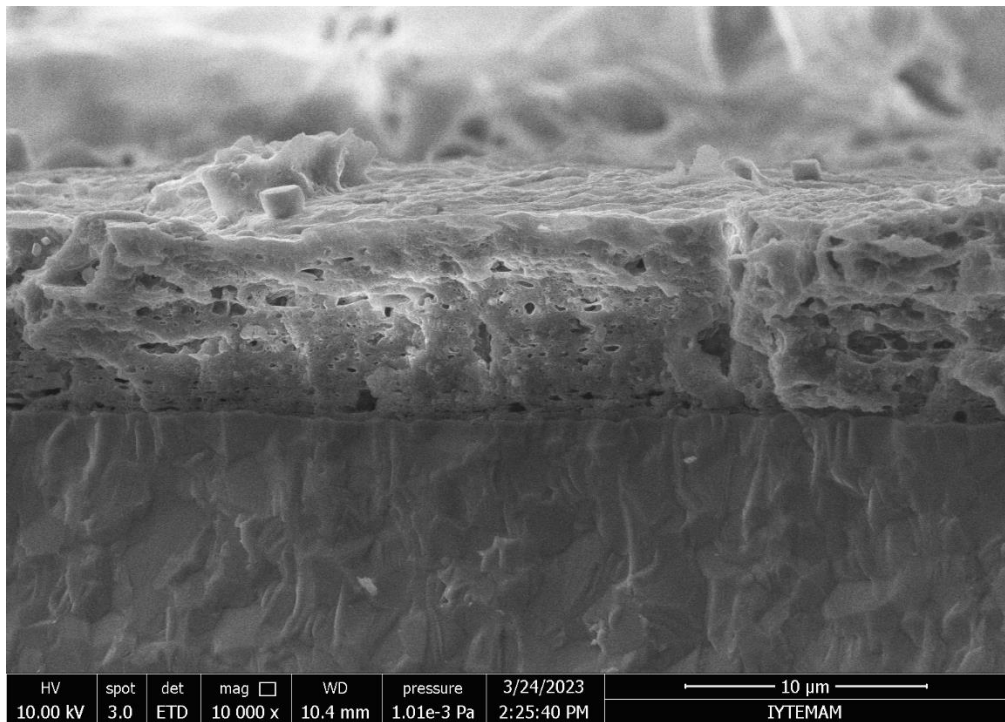


Figure 3.18. Cross-sectional SEM Image of Coated GDC Pellet by Solution F

3.7. X-Ray Diffraction Analysis of Coatings

After the coating experiments, XRD analyses were performed on the pellets. XRD analyses were performed to see the phases formed at 700 °C, which is the temperature during EIS measurements. Since the signals came not only from the coating but also from the underlying GDC ceramic pellet, the GDC peaks were dominant in the XRD analysis results. The coated pellets were kept in the box kiln for 2 hours at 700°C with 3 °C heating/cooling rate, which was determined as one of the intermediate temperature solid oxide fuel cell operating temperatures. In order to avoid the formation of dominant GDC peaks, these coatings were scraped from the GDC pellets and XRD analyses were performed. LSFCr and LCFCr multiphase peaks were not observed in the obtained results. After that, the pellets were kept for 2 hours at 900 °C with the same heating/cooling rate according to the studies in the literature. The coatings were scraped and XRD analyses were performed again. It has been observed that the desired peaks still do not occur. Thus, it can be said that 900 °C is also insufficient for the formation of LSFCr and LCFCr peaks in XRD results. Considering the long operation times of the SOFC cell at temperatures around 700 °C, these new mixed oxides may be expected to eventually form. Perhaps another reason can be that the stoichiometry in the prepared solutions is unmatching with desired values. Obtained XRD analysis results are shown below from A to H, respectively. Cu K α radiation was used in the analysis.

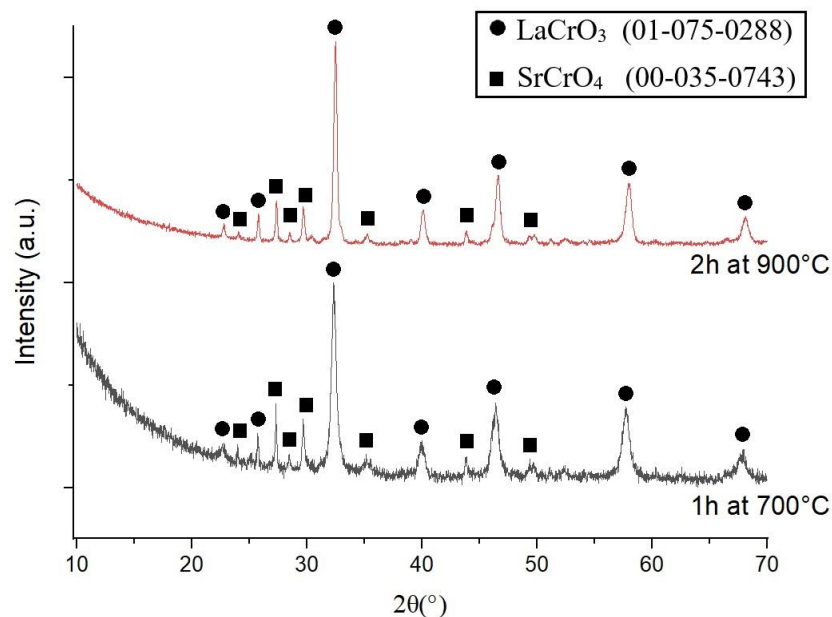


Figure 3.19. XRD Analysis Chart of Coating made by Solution A

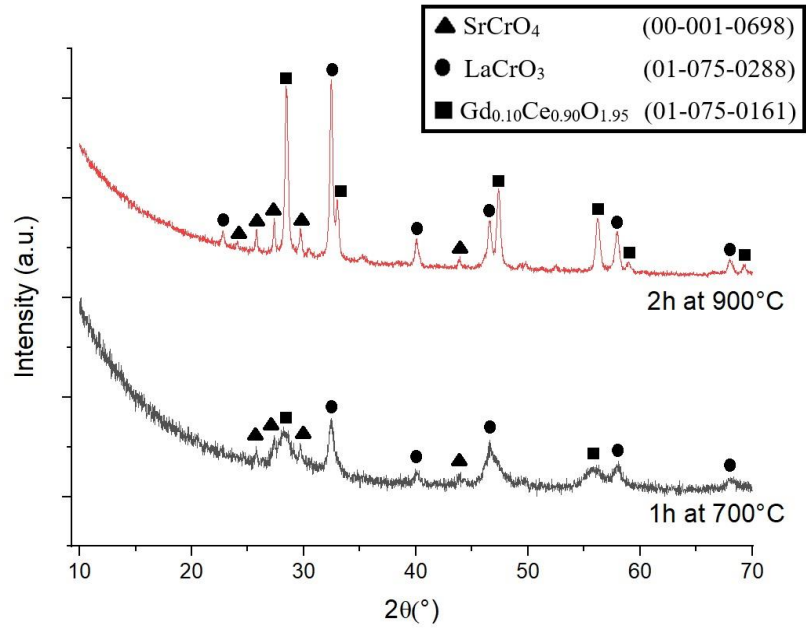


Figure 3.20. XRD Analysis Chart of Coating made by Solution B

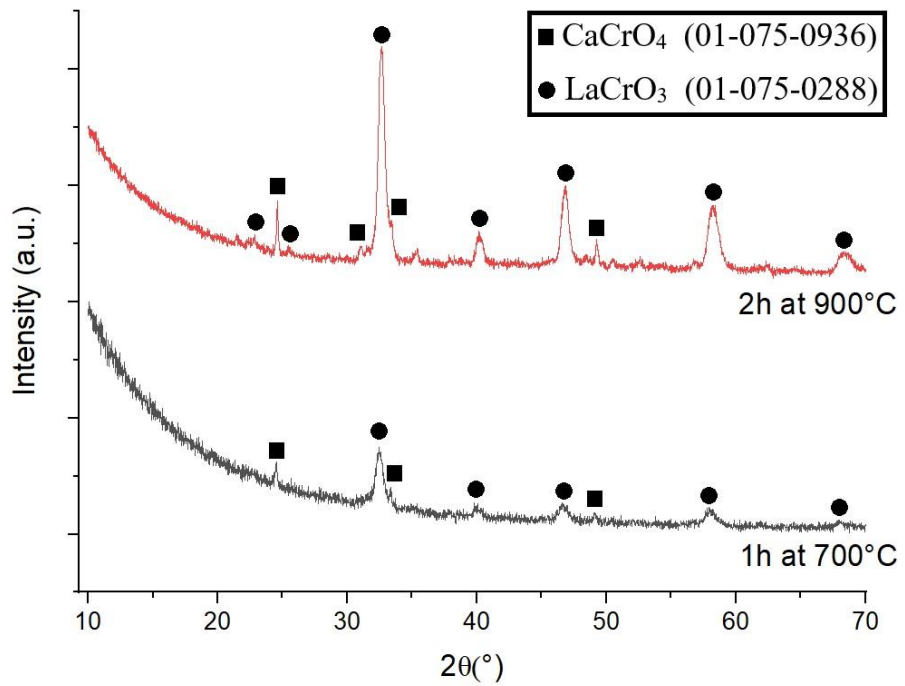


Figure 3.21. XRD Analysis Chart of Coating made by Solution C

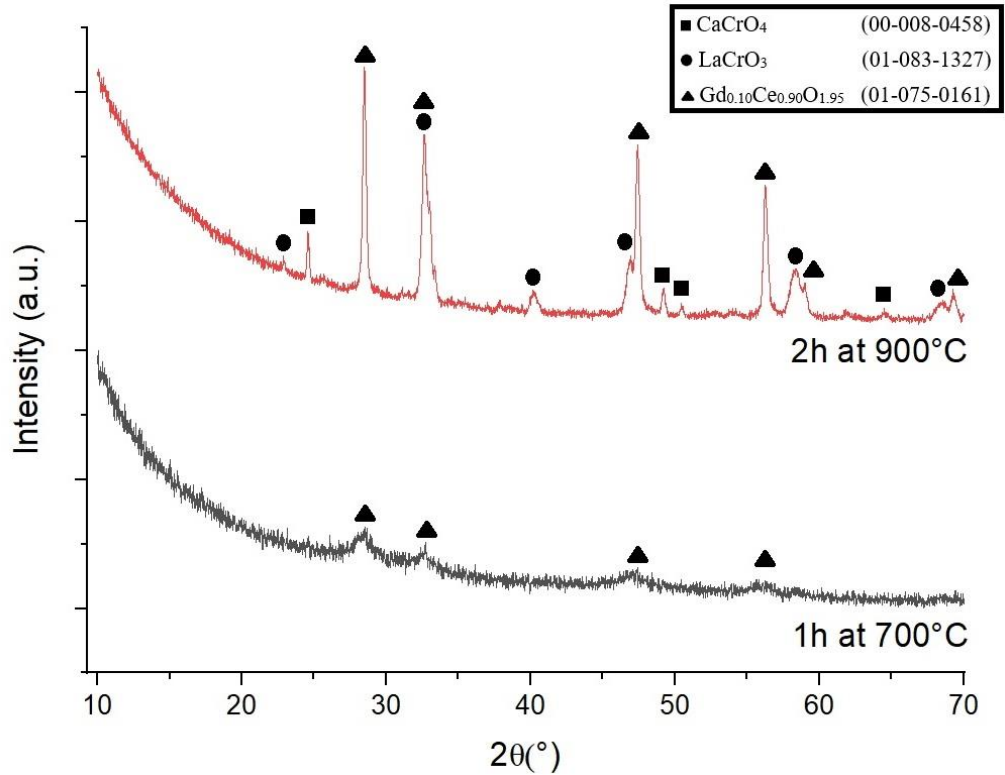


Figure 3.22. XRD Analysis Chart of Coating made by Solution D

The XRD results in thesis were obtained by keeping the coatings at 700 and 900 °C. According to the results in this article, XRD analysis of the coating made with solution E was done without heating and scraping in Figure 3.23a. Due to the nature of the measurement geometry XRD signal from the electrolyte was dominant in the coated sample and peaks from the coating layer were relatively overshadowed. However, SrNO_3 salt was also detected in the coating layer. Because the spray coating process was done at 300 °C and this salt was expected from the literature^[43]. The coating made by Solution E is scraped off from the electrolyte surface and heated at 700 °C for 2h in an electric kiln to perform operation conditions and the XRD results is shown in Figure 3.23b.

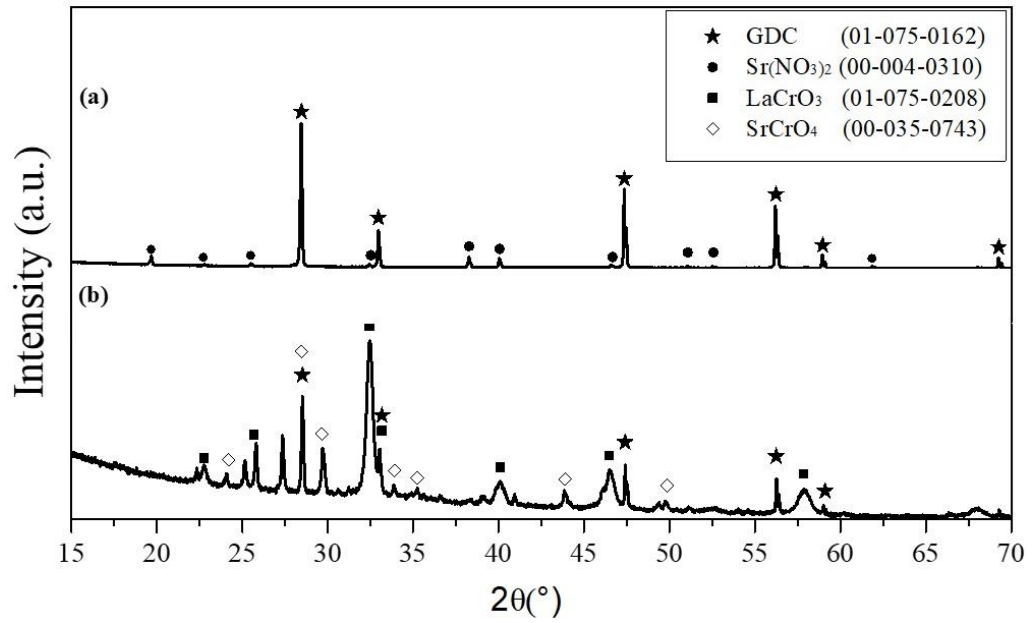


Figure 3.23. XRD Analysis Chart for (a) coating made by Solution E on GDC Pellet, (b) scraped coating made by Solution E and separately heated at 700 °C for 2 hours [66]

In Figure 3.24, the chart of XRD results obtained after the E solution was kept at 900 °C for 2 hours is shown.

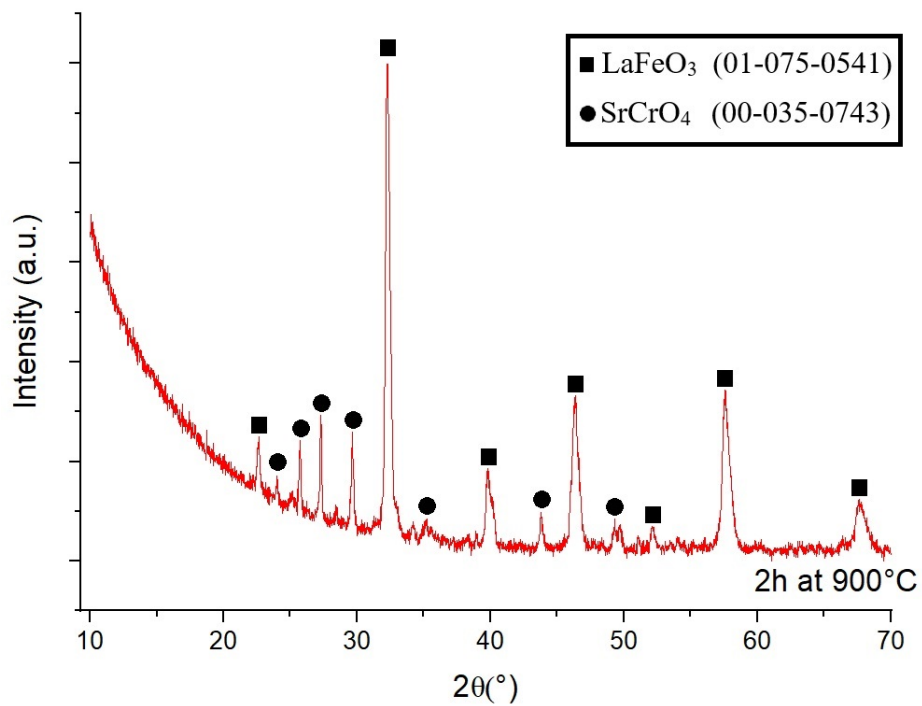


Figure 3.24. XRD Analysis Chart of Coating made by Solution E

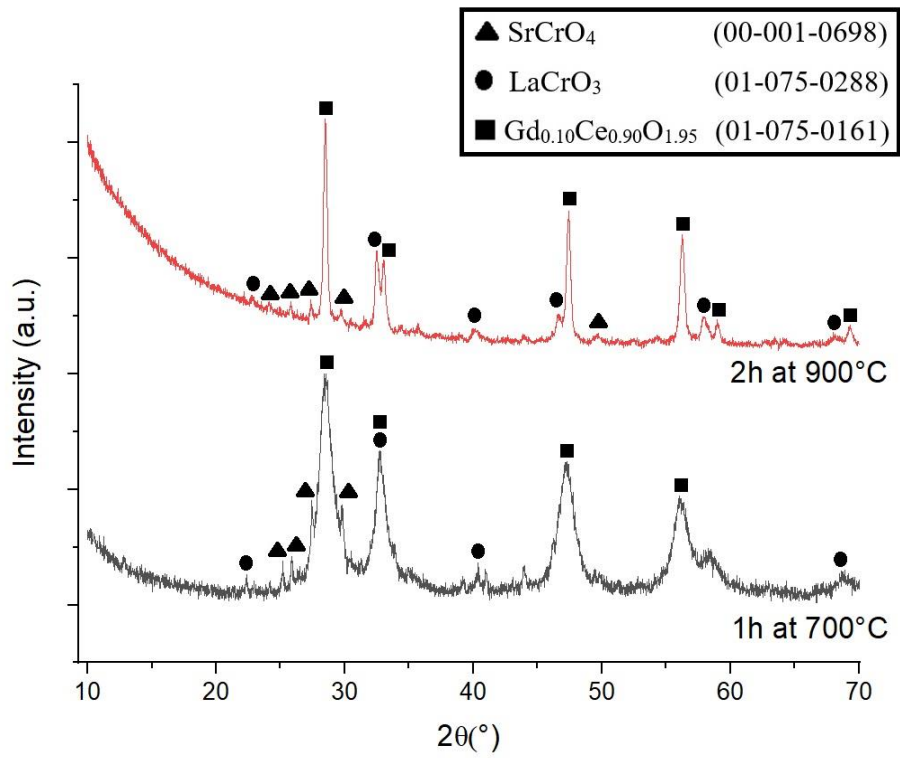


Figure 3.25. XRD Analysis Chart of Coating made by Solution F

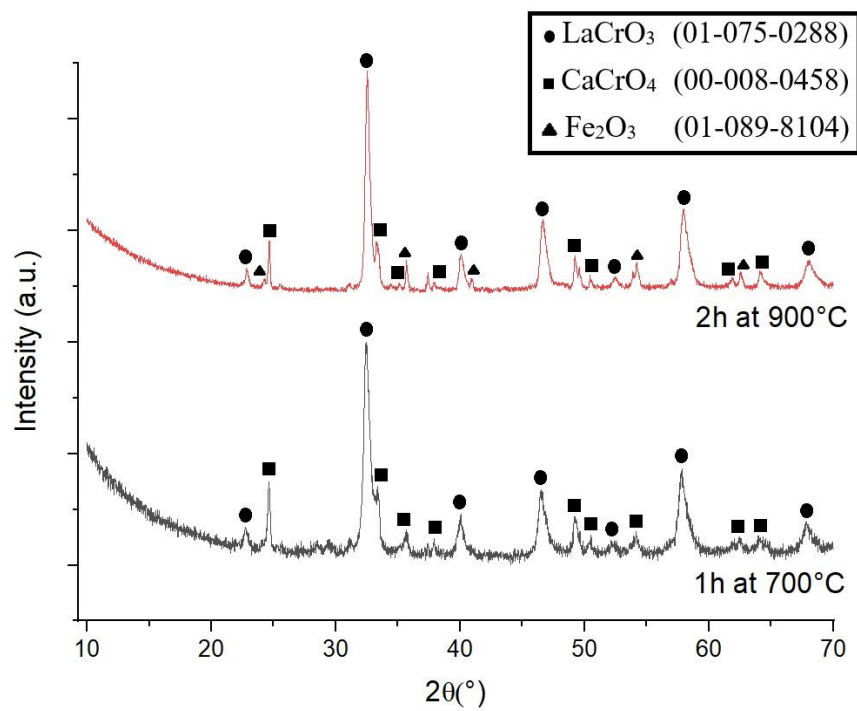


Figure 3.26. XRD Analysis Chart of Coating made by Solution G

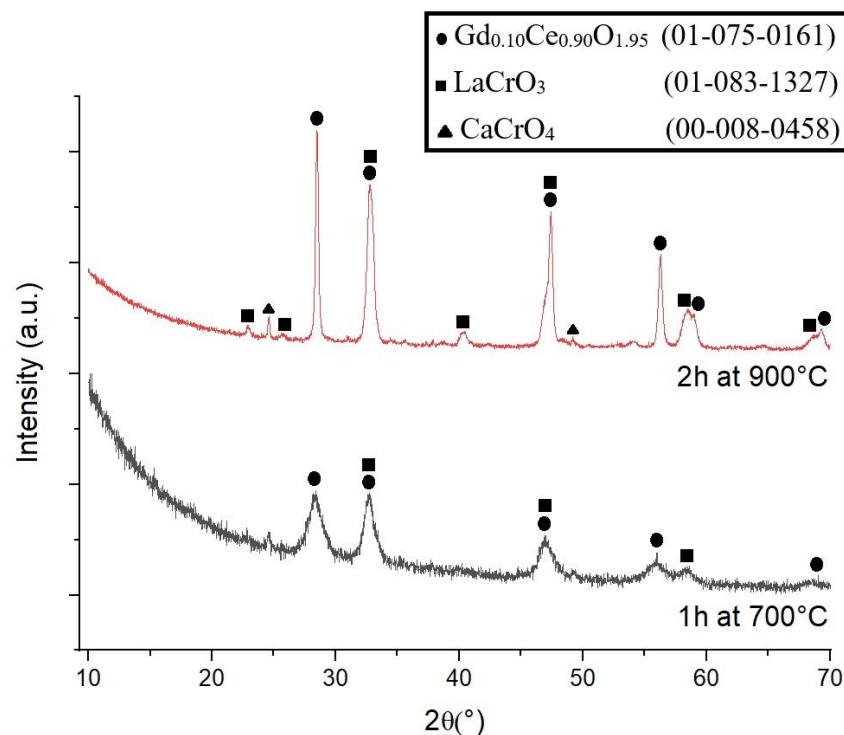


Figure 3.27. XRD Analysis Chart of Coating made by Solution H

After post heat treatments at 700 °C and 900 °C, multi-phase peaks such as LaSrFeCr and LaCaFeCr were not observed in XRD analyses results. It has been observed that compounds such as LaCrO₃, SrCrO₄ are formed instead mentioned multi-phases previously. In the literature, it has been determined that 900 °C, where similar multi-phase peaks occur, may also be insufficient.

3.8. Electrochemical Impedance Spectroscopy (EIS) Results

Electrochemical performance analyses were done with prepared symmetrical half-cells in Coating (Electrode) / Ceramic pellet (GDC Electrolyte) / Coating (Electrode) configuration. Impedance responses of symmetrical half-cells were shown as Nyquist and Bode plots. There are two parallel resistors which are connected to constant phase element (ASR2CPE2 and ASR3CPE3) and a serial resistor (ASR1) in the equivalent circuit. Serial resistor (ASR1) is the resistance to oxygen transport through the ceramic pellet (GDC Electrolyte) and any additional current collection resistances. ASR2 and ASR3 are resistances in electrochemical processes which are done at high and low

frequencies, respectively. The polarization resistances of 2 electrodes in the symmetrical half-cell is calculated with the sum of ASR2 and ASR3. It can be shown as ASR_{total} . ASR_{total} is divided by 2 to find the polarization resistance of single electrode ($ASR_{electrode}$). $ASR_{electrode}$ values were used in plots for comparison in EIS measurements of solutions A to H. Among the obtained results, ASR values of coated layers made by A, E and G solutions are desirable. Other results were found to be higher than the studies in the literature. In this regard, there may have been errors in coatings, silver paste application, EIS measurements. Impedance response measurements were taken at 500 °C, 550 °C, 600 °C, 650 °C and 700 °C in stagnant air. The "up" sign on the graphs refers to the measurement taken after the temperature increase, and the "down" refers to the measurement taken after the temperature decrease. For example, if the measurement has the expression "700 up", it means the measurement taken by bringing temperature from 650 °C to 700 °C. The bode plots drawn for A, E and G, which have desirable values obtained, can be used to observe different frequencies (from low to high). Fitting of impedance data is shown in both Bode and Nyquist plots. Capacitance, area specific resistance and summit frequency values can be extracted from $C=(ASR \times P)^{(1/n)}/ASR$ and $f=1/(2\pi \times ASR \times C)$ where p and n are fit parameters. In the optimization part of the experiment parameters, it was found that the best conditions were found in the 16th sample by using the E solution. In this optimization part, a detailed analysis of the half cell made by solution E was done. The high frequency process, defined by ASR2-CPE2 was associated with capacitances around 10^{-4} F/cm² over the temperature range of 550-700 °C (Table 3.10). The small capacitances observed, combined with the relatively high values of 'n' that indicate semi-circular patterns [82,83], imply that the high-frequency phenomenon involves oxygen transfer at the interface between the LSFcr electrode and GDC electrolyte. The rate at which oxygen is transferred at this electrode/electrolyte interface is likely influenced by the oxygen ion conductivity of GDC. Therefore, the similar activation energies of ASR1 (oxygen transport through the GDC electrolyte) and of ASR2 (Figure 3.28b) further supports our hypothesis that ASR2 indicated the rate of oxygen transfer at the electrode/electrolyte interface. ASR3 is associated with capacitances of ca. 10^{-3} F/cm² in the 550-700 °C temperature range (Table 3.10) and a relatively high activation energy of 1.50 eV (Figure 3.28b). In other MIEC electrodes that have been studied more frequently than LCFcr, such as; (La, Sr)CoO₃ and (La, Sr)(Co,Fe)O₃ films, the reported capacitance values associated with the low frequency rate-limiting step varied depending on the microstructure [31,37,84-90]. For example, MIEC

electrodes that had dense microstructures were reported to exhibit a low-frequency rate limiting processes with associated capacitances of 10^{-2} – 10^0 F/cm² [31,37,84-86]. On the other hand, EIS measurements performed on porous MIEC cathodes yielded rate limiting low frequency responses with capacitances of 10^{-4} – 10^{-3} F/cm², which is in the range of what has been observed in the present case [86-90]. Regardless the capacitance value, all the rate limiting low frequency values were ascribed to oxygen exchange at the electrode surface [31,37,84-90].

One potential reason for the apparent inconsistency could be attributed to the level of lattice participation, influenced by variations in the microstructure. For instance, electrodes with porosity offer numerous surfaces where oxygen can be adsorbed, spread throughout the electrode. As a result, oxygen adsorption can occur across extensive surface areas, including those in proximity to the electrolyte. In this situation, the oxygen that is adsorbed may be transported to the electrolyte through both the surface and the bulk of the electrode. Alternatively, when it comes to dense electrodes, oxygen adsorption predominantly occurs on the upper surface of the electrode, necessitating the use of the bulk pathway to reach the electrolyte. As a result, oxygen reduction relies more heavily on the lattice in dense MIEC (Mixed Ionic-Electronic Conductor) electrodes, in contrast to porous ones. This leads to a greater chemical capacitance in dense electrodes [91,92]. The relatively low capacitances of ca. 10^{-3} F/cm² obtained in the rate limiting low frequency process detected by the EIS measurements of the ESD-derived LCFCr cathodes in the present case is therefore, likely caused by the large surface area enabled by the porous microstructure. Another aspect of the surface oxygen adsorption-related chemical capacitance is that its magnitude depends on the amount of B-site transition metal cations that may be oxidized in response to the oxygen ion replacement by the oxygen vacancy [93]. As a result, the capacitance is influenced by the overall volume of the electrode, indicating a correlation between capacitance and electrode size. In this specific scenario, the lower capacitance value at low frequencies observed in the ESD-derived porous LSFcr, when compared to the porous LCFCr fabricated through the sintering of screen-printed powders, can be attributed to the dissimilarities in their thicknesses. The thinner coatings obtained here (thickness of ca. 6 μ m) contain smaller amounts of transition metal cations to be oxidized upon oxygen adsorption onto the electrode surface in comparison to those present in the 25 μ m-thick electrode in the work by Molero-Sanchez et al. [94], yielding smaller capacitances. Table 3.10 shows the results of the equivalent circuit fittings performed on impedance data collected at 550-700 °C. At 700 °C, an $ASR_{\text{electrode}}$

value of $0.26 \Omega \cdot \text{cm}^2$ was obtained. In the literature, Molero-Sanchez et al. fabricated $\text{La}_{0.3}\text{Ca}_{0.7}\text{Fe}_{0.7}\text{Cr}_{0.3}\text{O}_{3-\delta}$ (LCFCr) electrodes by depositing a paste containing the combustion-derived powders onto GDC electrolytes and sintering them at $1000 \text{ }^\circ\text{C}$ [42]. The electrode yielded an $\text{ASR}_{\text{electrode}}$ value of $0.73 \Omega \cdot \text{cm}^2$ at $700 \text{ }^\circ\text{C}$, which roughly corresponds to three times the $\text{ASR}_{\text{electrode}}$ value obtained here from ESD-derived LSFcr electrodes. In another study, Molero-Sanchez et al., fabricated LCFCr electrodes by a microwave-based methods, which yielded an $\text{ASR}_{\text{electrode}}$ value of $0.25 \Omega \cdot \text{cm}^2$, but at $800 \text{ }^\circ\text{C}$ [95]. Utilizing the optimized ESD method to fabricate a comparable LSFcr electrode evidently reduced the operating temperature by $100 \text{ }^\circ\text{C}$, without any loss in electrochemical performance. $\text{ASR}_{\text{electrode}}$ of solution A at $700 \text{ }^\circ\text{C}$ is found as $0.34 \Omega \cdot \text{cm}^2$ and $\text{ASR}_{\text{electrode}}$ of solution G at $700 \text{ }^\circ\text{C}$ is found as $0.29 \Omega \cdot \text{cm}^2$. The $\text{ASR}_{\text{electrode}}$ of solution A is found at 700 Up process, The $\text{ASR}_{\text{electrode}}$ of solution G is found at 700 Down process.

The Table 3.10 and Figure 3.28 are the EIS measurement results obtained from the symmetrical half-cell covered with the sample 16 parameters by solution E during the optimization of the ESD parameters.

Table 3.10. Summary of area specific resistance, capacitance and summit frequency. Errors associated with the ASR, P and n parameters determined through the equivalent circuit fittings were below 15% [66].

Temp ($^\circ\text{C}$)	ASR1 ($\Omega \cdot \text{cm}^2$)	ASR2 ($\Omega \cdot \text{cm}^2$)	ASR3 ($\Omega \cdot \text{cm}^2$)	P2	n2	C2 (F/cm^2)	f2 (Hz)	P3	n3	C3 (F/cm^2)	f3 (Hz)
700	3.21	0.2	0.314	0.00417	0.81	7.79E-04	1020	0.00889	0.88	4.06E-03	125
650	4.671	0.319	0.797	0.00238	0.85	6.71E-04	744	0.0066	0.8	3.40E-03	59
600	7.15	0.45	2.45	0.0013	0.9	5.69E-04	622	0.008	0.8	3.00E-03	22
550	11.7	0.74	7.7	0.0012	0.83	2.85E-04	756	0.0056	0.77	2.19E-03	9

The $\text{ASR}_{\text{electrode}}$ values obtained from the samples by coating the solutions prepared from A to H with sample 16 experimental parameters are shown in the Table 3.11. The $\text{ASR}_{\text{electrode}}$ value refers to the ASR value of a single layer in the symmetrical cell.

Table 3.11. Obtained $ASR_{\text{electrode}}$ Values by Samples A to H

Sample Name	$ASR_{\text{electrode}}(\Omega.\text{cm}^2)$
A	0.34
B	1.81
C	1.25
D	4.76
E	0.22
F	46.14
G	0.29
H	0.81

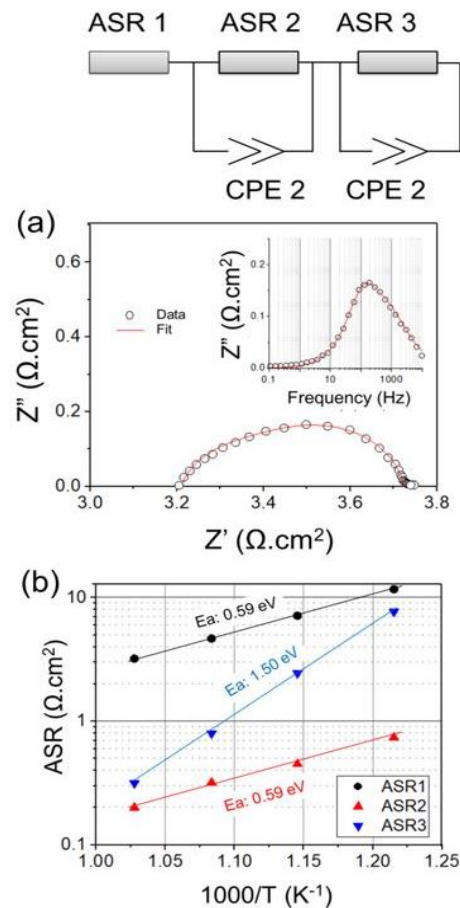


Figure 3.28. a) Impedance response of the symmetrical half cells with sample 16 electrodes, collected at 700 °C, in stagnant air. Equivalent circuit used to fit the impedance data is also provided above the Nyquist and Bode plots. b) Temperature dependence of the area specific resistance components of the overall impedance response, namely ASR1, ASR 2 and ASR 3 ^[66].

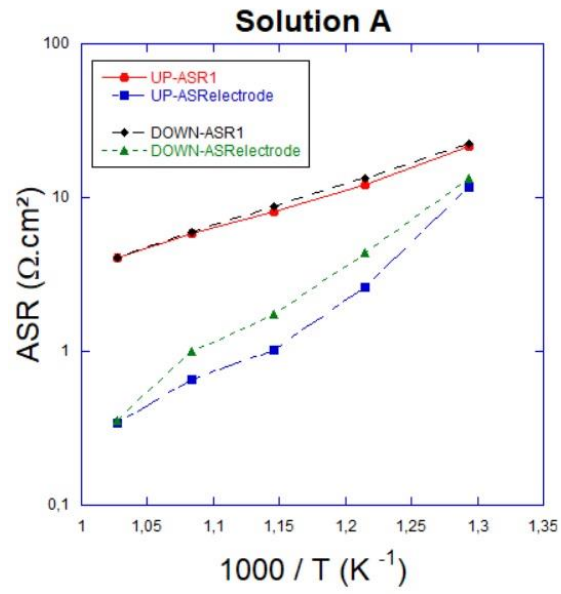


Figure 3.29. ASR_{electrode} Values of Symmetrical Half Cell Coated with Solution A

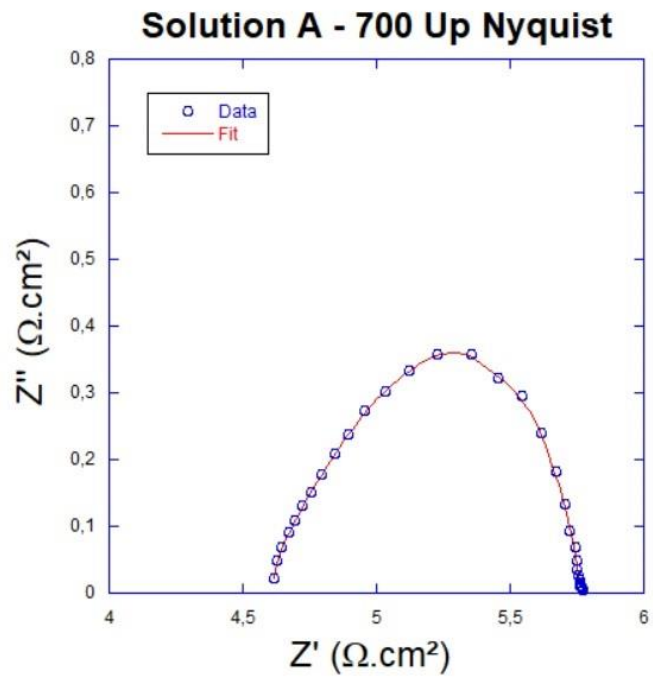


Figure 3.30. Nyquist Plot of 700 Up Process in EIS with Solution A Coated Symmetrical Half Cell

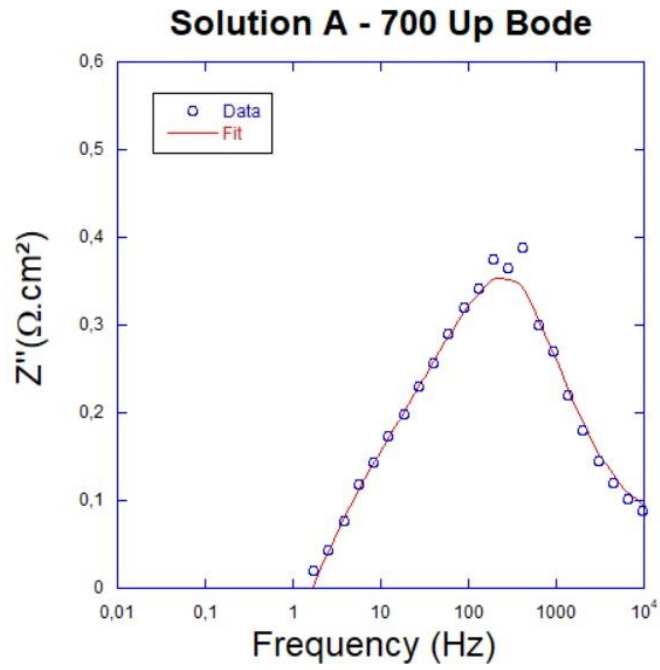


Figure 3.31. Bode Plot of 700 Up Process in EIS with Solution A Coated Symmetrical Half Cell

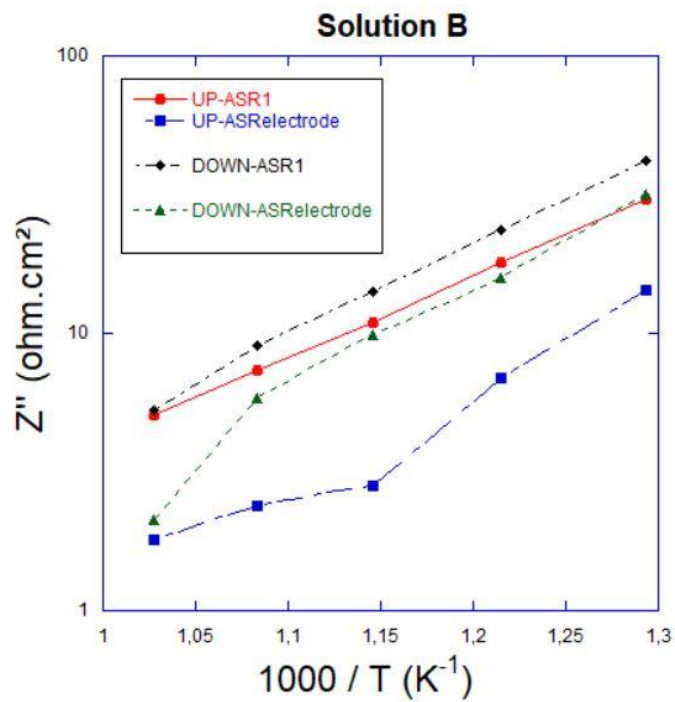


Figure 3.32. $ASR_{electrode}$ Values of Symmetrical Half Cell Coated with Solution B

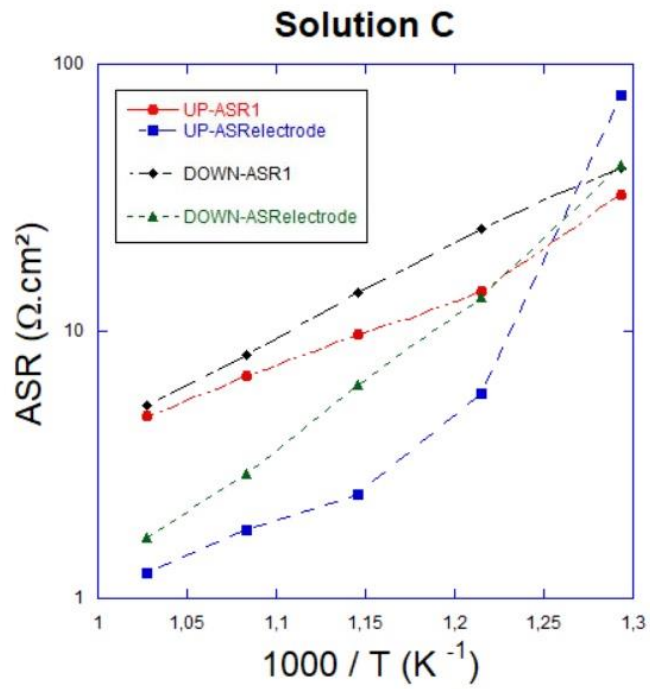


Figure 3.33. $ASR_{\text{electrode}}$ Values of Symmetrical Half Cell Coated with Solution C

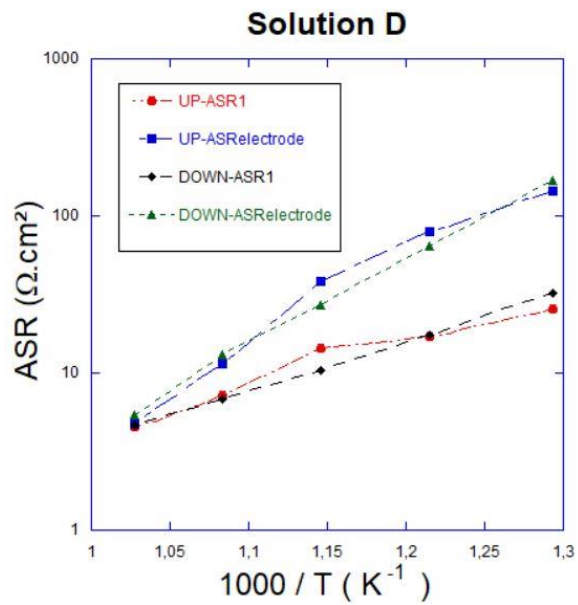


Figure 3.34. $ASR_{\text{electrode}}$ Values of Symmetrical Half Cell Coated with Solution D

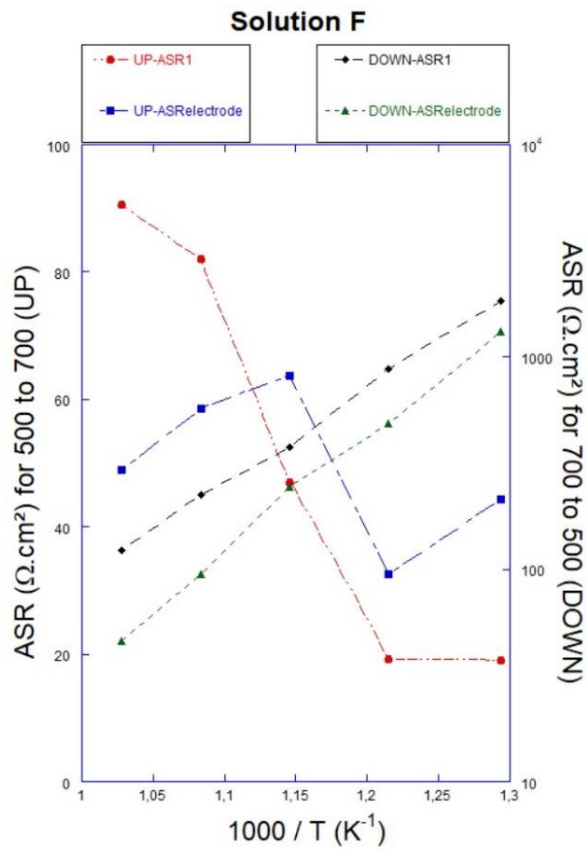


Figure 3.35. ASR_{electrode} Values of Symmetrical Half Cell Coated with Solution F

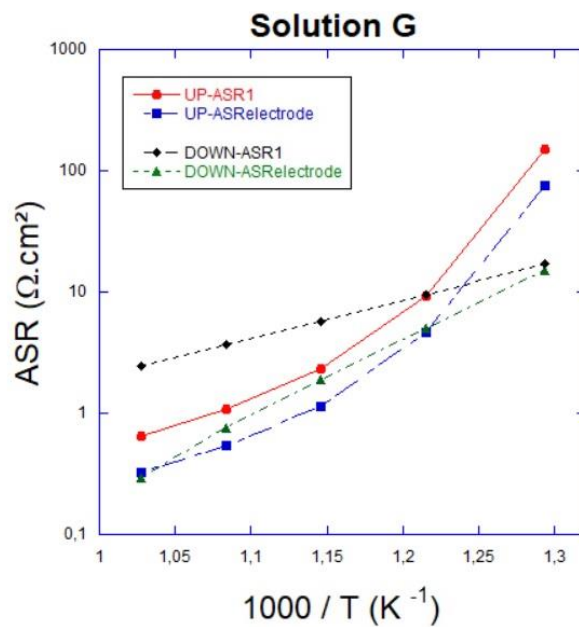


Figure 3.36. ASR_{electrode} Values of Symmetrical Half Cell Coated with Solution G

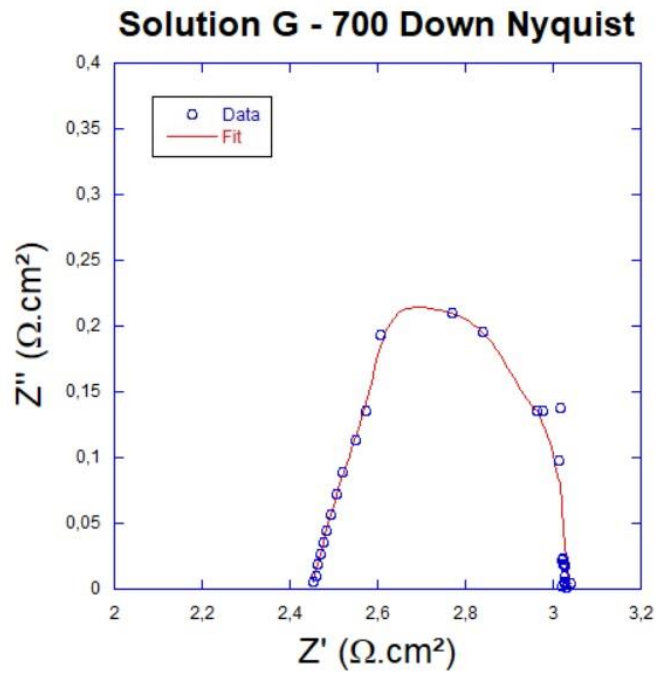


Figure 3.37. Nyquist Plot of 700 Down Process in EIS with Solution G Coated Symmetrical Half Cell

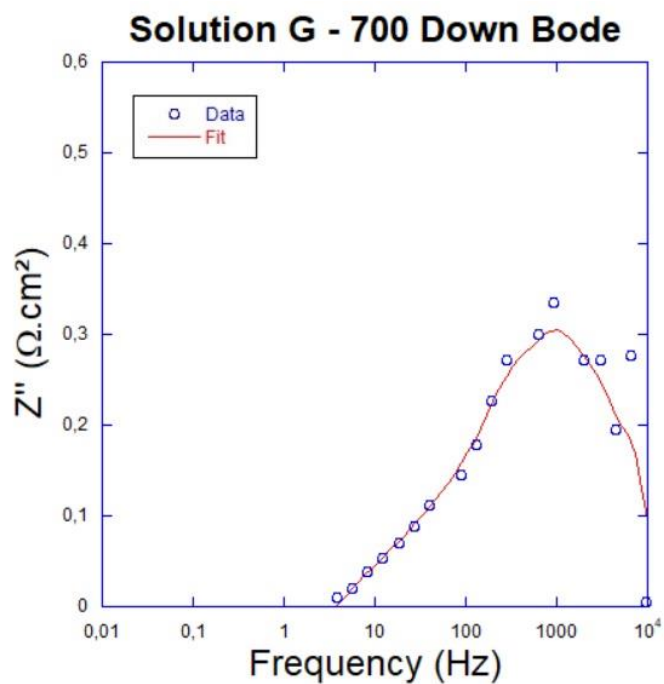


Figure 3.38. Bode Plot of 700 Down Process in EIS with Solution G Coated Symmetrical Half Cell

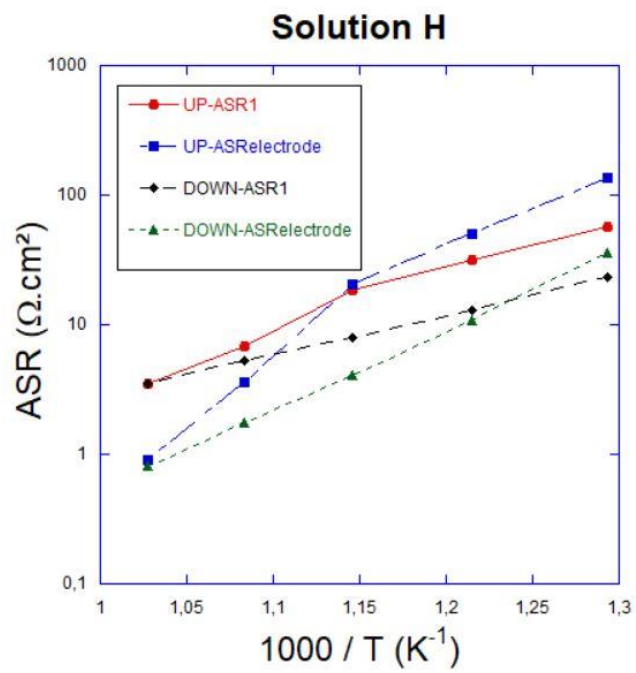


Figure 3.39. ASR_{electrode} Values of Symmetrical Half Cell Coated with Solution H

CHAPTER 4

CONCLUSION

LSFCr and LCFCr cathode layers were coated on GDC electrolyte by electrospray deposition (ESD) method. Plackett-Burman Design Method as statistical experimental design is used to find optimized ESD parameters for desired coating structure. Reticular structure is desired coating structure to obtain larger surface area. The best reticular structure was fabricated with sample 16 experimental parameters which are a flow rate of 0.01 ml/h, a voltage of 7 kV, a concentration of 0.004 M, a WD of 27mm, a temperature of 300 °C and a coating duration of 20 minutes. After optimization of ESD parameters part, solutions were changed and named as A to H for observing the effects of different precursor salts and solvents. These solutions were prepared with LSFCr, LCFCr, LSFCr-GDC and LCFCr-GDC combinations. Coatings were fabricated with using these solutions by sample 16 experimental parameters. It was observed that coatings made with solutions prepared using ethanol and butyl carbitol formed glassy, dense and thin coatings on the GDC pellet. It was determined that the coatings made with solutions prepared using Ethylene glycol and 2-Butoxyethanol had a partially thick and reticular (coral-like) structure. The coating that has the thinnest average thickness is made with solution D and it is 1.0 μm . Coating stoichiometries were incompatible with desired values. This situation was noticed at the last stages of the thesis studies. Although this situation causes problems such as peak formation in XRD results, undissolved particles in SEM images, etc., it has been observed that results similar to the literature were obtained in EIS measurement results. XRD results did not show LaSrFeCr or LaCaFeCr peaks, but instead showed compounds such as mostly LaCrO₃, SrCrO₄ peaks. This may be due to insufficient heat treatment temperatures which are 700 and 900 °C. EIS measurements showed favorable ASR values of 0.22 $\Omega\cdot\text{cm}^2$ at 700 °C for coating made by solution E. Coatings for solution A and G showed close EIS measurement results to literature as 0.34 and 0.29 $\Omega\cdot\text{cm}^2$, respectively. Contrary to the coating made with solution A, it was observed that the coatings made with solutions E and G had a reticular structure. The EIS measurement value obtained from the coating with solution F was much higher than expected. The reasons for this may be no contact between the coating and the silver paste,

the separation of the coating from the pellet while heating in the oven, the lack of contact between the wires while the circuit is being completed, etc.

REFERENCES

- [1] U.S. Department of Energy, Office of Energy Efficiency and Renewable Energy. (2013). Available from: <http://www.eere.energy.gov/>
- [2] Renewable energy – powering a safer future. (n.d.). Retrieved from <https://www.un.org/en/climatechange/raising-ambition/renewable-energy>
- [3] Delubac, A., Mar, 2023, What is Carbon Management? (N.d.). Retrieved from <https://greenly.earth/en-gb/blog/company-guide/what-is-carbon-management>
- [4] Causes of Climate Change, European Commission, (N.d.-a). Retrieved from https://climate.ec.europa.eu/climate-change/causes-climate-change_en
- [5] European Green Deal, European Parliament, Dec,2019, (N.d.-a). Retrieved from [https://www.europarl.europa.eu/RegData/etudes/ATAG/2019/644205/EPRS_ATA\(2019\)644205_EN.pdf](https://www.europarl.europa.eu/RegData/etudes/ATAG/2019/644205/EPRS_ATA(2019)644205_EN.pdf)
- [6] Fit for 55 - the EU's plan for a green transition – consilium, Council of the European Union, (N.d.-a). Retrieved from <https://www.consilium.europa.eu/en/policies/green-deal/fit-for-55-the-eu-plan-for-a-green-transition/>
- [7] Carbon Border Adjustment Mechanism, European Commission, (N.d.-a). Retrieved from https://taxation-customs.ec.europa.eu/carbon-border-adjustment-mechanism_en
- [8] Hydrogen Storage, Office of Energy Efficiency and Renewable Energy, (n.d.). Retrieved from <https://www.energy.gov/eere/fuelcells/hydrogen-storage>
- [9] Hydrogen Production by Dark Fermentation of Biomass Resources, European Commission, (N.d.-a). Retrieved from <https://cordis.europa.eu/>
- [10] Kirubakaran A., Shailendra J., Nema R.K. 2009. “A review on fuel cell technologies and power electronic interface”, *Renewable and Sustainable Energy Reviews*, 13(9), 2430-2440.
- [11] Coralli A., Sarruf B. J.M., de Miranda P. E. V., Osmieri L., Specchia S., Minh N. Q., Chapter 2 - Fuel Cells,, Editor(s): Paulo Emilio V. de Miranda, *Science and Engineering of Hydrogen-Based Energy Technologies*, Academic Press, 2019, Pages 39-122, ISBN 9780128142516

- [12] Steele B. C. H., 2001, "Material science and engineering: The enabling technology for the commercialisation of fuel cell systems", *Journal of Materials Science*, 36 (5), 1053-1068.
- [13] Gyan D.S., Gupta R., Roy P.K.. 2015. "Comparision of GDC electrolyte-LSCF cathode IT-SOFC system with conventional power sources", *IEEE*, 1-6.
- [14] Beckel D., Bieberle-Hütter A., Harvey A., Infortuna A., Muecke U.P., Prestat M., Rupp J.L.M., Gauckler J.L. 2007. "Thin films for micro solid oxide fuel cells", *Journal of Power Sources*, 173 (1), 325-345.
- [15] Steele B. C. H., 2000, "Materials for IT-SOFC stacks: 35 years R&D: the inevitability of gradualness", *Solid State Ionics*, 134 (1-2), 3-20.
- [16] Skinner S.J. Kilner J.A. 2003 "Oxygen ion conductors", *Materials Today*, 6(3), 30-37.
- [17] Gödickemeier, M. ve Gauckler, L.J., 1998, "Engineering of solid oxide fuel cells with ceria-based electrolytes", *Journal of the Electrochemical Society*, 145 (2), 414-421.
- [18] Ormerod R.M., 2003, "Solid Oxide Fuel Cells", *Chemical Society Review*, 32(1), 17-28
- [19] O'Hayre R., Cha S.W., Colella W., Prinz F.B., 2005, *Fuel Cell Fundamentals*, John Wiley & Sons, New York, USA
- [20] Bieberle H.A., Beckel D., Infortuna A., Muecke U. P., Rupp J. L.M., Gauckler L. J, Rey-Mermet S., Muralt P., Bieri N. R., Hotz N., Stutz M.J., Poulikakos D., Heeb P., Müller P., Bernard A., Gmür R., Hocker A., 2008. "A micro-solid oxide fuel cell system as battery replacement", *Journal of Power Sources*, 177(1), 123-130.
- [21] Special Section:Energy-Solid Oxide Fuel Cells and Membranes, *The Global Home of Chemical Engineers*, (2016). Retrieved from <https://www.aiche.org/resources/publications/cep/2016/july/special-section-energy-solid-oxide-fuel-cells-and-membranes>
- [22] Kosacki I., Suzuki T., Petrovsky V., Anderson H. U., 2000, "Electrical conductivity of nanocrystalline ceria and zirconia thin films", *Solid State Ionics*, 136–137, 1225-1233.
- [23] O'Hayre R., Cha S.W., Colella W., Prinz F.B., 2005, *Fuel Cell Fundamentals*, John Wiley & Sons, New York, USA
- [24] Cheng Z., Zha S., Meilin Liu, Influence of cell voltage and current on sulfur poisoning behavior of solid oxide fuel cells, *Journal of Power Sources*, Volume 172,

- Issue 2, 2007, Pages 688-693, ISSN 0378-7753,
<https://doi.org/10.1016/j.jpowsour.2007.07.052>.
- [25] Neelima M., Amitava B., Alka G., Shobit O., Kantesh B., Progress in material selection for solid oxide fuel cell technology: A review, *Progress in Materials Science*, Volume 72, 2015, Pages 141-337, ISSN 0079-6425, <https://doi.org/10.1016/j.pmatsci.2015.01.001>.
- [26] F. Ramadhani, M.A. Hussain, H. Mokhlis, S. Hajimolana, Optimization strategies for Solid Oxide Fuel Cell (SOFC) application: A literature survey, *Renewable and Sustainable Energy Reviews*, Volume 76, 2017, Pages 460-484, ISSN 1364-0321, <https://doi.org/10.1016/j.rser.2017.03.052>.
- [27] Buyukaksoy A., Petrovsky V., Dogan F., “Redox Stability of Ni-YSZ Cermets Prepared by Polymeric Precursor Infiltration” *ECS Transactions* 45 (2012) 509. DOI:10.1149/1.3701342
- [28] Buyukaksoy A., Petrovsky V., Dogan F., “Optimization of Redox Stable Ni-YSZ Anodes for SOFCs by Two-Step Infiltration” *Journal of The Electrochemical Society* 159 (2012) F841. DOI: 10.1149/2.075212jes
- [29] A.Buyukaksoy, V. Petrovsky, F. Dogan “Stability and Performance of Solid Oxide Fuel Cells with Nanocomposite Electrodes” *Journal of The Electrochemical Society* 159 (2012) B666. DOI: 10.1149/2.050206jes
- [30] Tai L.W., Nasrallah M.M., Anderson H.U., Sparlin D.M., Sehlin S.R., 1995, “Structure and electrical properties of $\text{La}_{1-x}\text{Sr}_x\text{Co}_{1-y}\text{Fe}_y\text{O}_3$. Part 1. The system $\text{La}_{0.8}\text{Sr}_{0.2}\text{Co}_{1-y}\text{Fe}_y\text{O}_3$ ”, *Solid State Ionics* 76, 259-271
- [31] Tai L.W., Nasrallah M.M., Anderson H.U., Sparlin D.M., Sehlin S.R., 1995, “Structure and electrical properties of $\text{La}_{1-x}\text{Sr}_x\text{Co}_{1-y}\text{Fe}_y\text{O}_3$. Part 2. The system $\text{La}_{1-x}\text{Sr}_x\text{Co}_{0.2}\text{Fe}_{0.8}\text{O}_3$ ”, *Solid State Ionics* 76, 273-283
- [32] Chen M., Paulson S., Thangadurai V., Birss V., 2013, “Sr-rich chromium ferrites as symmetrical solid oxide fuel cell electrodes”, *Journal of Power Sources* 236, 68-79.
- [33] Addo P., Molero-Sanchez B., Buyukaksoy A., Paulson S., Birss V., 2015, “Sulfur tolerance of $\text{La}_{0.3}\text{M}_{0.7}\text{Fe}_{0.7}\text{Cr}_{0.3}\text{O}_{3-\delta}$ (M=Sr, Ca) solid oxide fuel cell anodes”, *ECS Transactions*, 66 (2), 219-228.
- [34] Addo P.K., Molero-Sanchez B., Chen M., Paulson S., Birss V., 2015, “CO/CO₂ study of high performance $\text{La}_{0.3}\text{Sr}_{0.7}\text{Fe}_{0.7}\text{Cr}_{0.3}\text{O}_{3-\delta}$ reversible SOFC electrodes”, *Fuel Cells* 15 (5) 689-696.

- [35] Marinha D., Dessemond L., J. Scott Cronin, James R. Wilson, Scott A. Barnett, and Elisabeth Djurado *Chemistry of Materials* 2011 23 (24), 5340-5348 DOI: 10.1021/cm2016998
- [36] Çelikbilek Ö., Siebert E., David Jauffrès, Christophe L. Martin, Elisabeth Djurado, Influence of sintering temperature on morphology and electrochemical performance of LSCF/GDC composite films as efficient cathode for SOFC, *Electrochimica Acta*, Volume 246, 2017, Pages 1248-1258, ISSN 0013-4686, <https://doi.org/10.1016/j.electacta.2017.06.070>.
- [37] Marinha D., Dessemond L., Djurado E., Electrochemical investigation of oxygen reduction reaction on $\text{La}_{0.6}\text{Sr}_{0.4}\text{Co}_{0.2}\text{Fe}_{0.8}\text{O}_{3-\delta}$ cathodes deposited by Electrostatic Spray Deposition, *Journal of Power Sources*, Volume 197, 2012, Pages 80-87, ISSN 0378-7753, <https://doi.org/10.1016/j.jpowsour.2011.09.049>.
- [38] Marinha D., Hayd J., Dessemond L., E. Ivers-Tiffée, Djurado E., Performance of $(\text{La,Sr})(\text{Co,Fe})\text{O}_{3-x}$ double-layer cathode films for intermediate temperature solid oxide fuel cell, *Journal of Power Sources*, Volume 196, Issue 11, 2011, Pages 5084-5090, ISSN 0378-7753, <https://doi.org/10.1016/j.jpowsour.2011.01.063>.
- [39] Marinha D., Rossignol C., Djurado E., Influence of electro spraying parameters on the microstructure of $\text{La}_{0.6}\text{Sr}_{0.4}\text{Co}_{0.2}\text{Fe}_{0.8}\text{O}_{3-\delta}$ films for SOFCs, *Journal of Solid State Chemistry*, Volume 182, Issue 7, 2009, Pages 1742-1748, ISSN 0022-4596, <https://doi.org/10.1016/j.jssc.2009.04.018>.
- [40] J. Sar, F. Charlot, A. Almeida, L. Dessemond, E. Djurado, Volume 14, Issue 3 Special Issue: Fundamentals & Developments of Fuel Cells Conference 2013 (FDFC2013) June, 2014 Pages 357-363
- [41] Marinha D., Dessemond L., and Djurado E., “Microstructure-Electrical Properties of Original LSCF Films Deposited by ESD for IT-SOFCs,” *ECS Trans.*, vol. 28, no. 11, pp. 93–103, 2019, doi: 10.1149/1.3495835.
- [42] Marinha, D., Dessemond, L., & Djurado, E. (2011). Comparison of electrochemical performances of electro sprayed lscf cathode films for it-sofcs for different morphologies and cobalt contents. *ECS Transactions*, 35(1), 2283.
- [43] Sındıraç C., Akkurt S., Microstructural investigation of the effect of electro spraying parameters on LSCF films, *International Journal of Hydrogen Energy*, Volume 45, Issue 60, 2020, Pages 35139-35148, ISSN 0360-3199, <https://doi.org/10.1016/j.ijhydene.2020.02.194>.

- [44] Addo, P., Mulmi, S., Molero-Sánchez, B., Keyvanfar, P., Thangadurai, V., & Birss, V. (2016, September). Performance Enhancement of $\text{La}_{0.3}\text{Sr}_{0.7}\text{Fe}_{0.7}\text{Cr}_{0.3}\text{O}_{3-\delta}$ (LSFCr) Electrodes in CO_2/CO Atmosphere. In ECS Meeting Abstracts (No. 40, p. 3041). IOP Publishing.
- [45] Chen M.; Chen D.; Chang M.; Hu H.; Xu Q. New Insight into Hydrogen Oxidation Reaction on $\text{La}_{0.3}\text{Sr}_{0.7}\text{Fe}_{0.7}\text{Cr}_{0.3}\text{O}_{3-\delta}$ Perovskite as a Solid Oxide Fuel Cell Anode. *J. Electrochem. Soc.* 2017, 164, F405–F411. DOI: 10.1149/2.1571704jes.
- [46] Kozokaro, V. F., Addo, P. K., Ansari, H. M., Birss, V. I., & Toroker, M. C. (2020). Optimal Oxygen Vacancy Concentration for CO_2 Reduction in LSFCr Perovskite: A Combined Density Functional Theory and Thermogravimetric Analysis Measurement Study. *The Journal of Physical Chemistry C*, 124(50), 27453-27466.
- [47] Molero-Sanchez, B.; Addo, P.; Buyukaksoy, A.; Paulson, S.; Birss, V. *Faraday Discussions* 2015, 182, 159-175.
- [48] Celikbilek Ö, Jauffrès D, Siebert E, Dessemond L, Burriel M, Martin CL, Djurado E, 2016, "Rational design of hierarchically nanostructured electrodes for solid oxide fuel cells", *Journal of Power Sources* 333, 72–82.
- [49] A. El-Himri, Marrero-López, D., , J. C. Ruiz-Morales, J. Peña-Martínez, and P. Núñez, "Structural and electrochemical characterisation of $\text{Pr}_{0.7}\text{Ca}_{0.3}\text{Cr}_{1-y}\text{Mn}_y\text{O}_{3-\delta}$ as symmetrical solid oxide fuel cell electrodes," *Journal of Power Sources*, vol. 188, no. 1, pp. 230-237, 2009.
- [50] X. Tong, Y. Xu, Đ. Tripković, P. V. Hendriksen, W.-R. Kiebach, and M. Chen, "Promotion of oxygen reduction and evolution by applying a nanoengineered hybrid catalyst on cobalt free electrodes for solid oxide cells," *Journal of Materials Chemistry A*, vol. 8, no. 18, pp. 9039–9048, 2020.
- [51] H. Tong, M. Fu, Y. Yang, F. Chen, and Z. Tao, "A novel self-assembled Cobalt-free perovskite composite cathode with triple-conduction for intermediate proton-conducting solid oxide fuel cells," *Advanced Functional Materials*, vol. 32, no. 48, p. 2209695, 2022.
- [52] L. R. Tarutina, G. K. Vdovin, J. G. Lyagaeva, and D. A. Medvedev, "Comprehensive analysis of oxygen transport properties of a $\text{BaFe}_{0.7}\text{Zr}_{0.2}\text{Y}_{0.1}\text{O}_{3-\delta}$ -based mixed Ionic-electronic conductor," *Journal of Membrane Science*, vol. 624, p. 119125, 2021.
- [53] Y.-D. Kim, J.-Y. Yang, M. Saqib, K. Park, J.-seop Shin, M. Jo, K. M. Park, H.-T. Lim, S.-J. Song, and J.-Y. Park, "Cobalt-free perovskite $\text{Ba}_{1-x}\text{Nd}_x\text{FeO}_{3-\delta}$ air electrode

- materials for reversible solid oxide cells,” *Ceramics International*, vol. 47, no. 6, pp. 7985–7993, 2021.
- [54] J. Peña-Martínez, D. Marrero-López, D. Pérez-Coll, J. C. Ruiz-Morales, and P. Núñez, “Performance of XSCOF (x=Ba, La and Sm) and LSCrX' (X'=Mn, Fe and Al) perovskite-structure materials on LSGM electrolyte for it-SOFC,” *Electrochimica Acta*, vol. 52, no. 9, pp. 2950–2958, 2007.
- [55] W. Zhou, Z. Shao, R. Ran, P. Zeng, H. Gu, W. Jin, and N. Xu, “Ba_{0.5}Sr_{0.5}Co_{0.8}Fe_{0.2}O_{3-δ}+LaCoO₃ composite cathode for Sm_{0.2}Ce_{0.8}O_{1.9}-electrolyte based intermediate-temperature solid-oxide fuel cells,” *Journal of Power Sources*, vol. 168, no. 2, pp. 330–337, 2007.
- [56] D. Chen, C. Huang, R. Ran, H. J. Park, C. Kwak, and Z. Shao, “New Ba_{0.5}Sr_{0.5}Co_{0.8}Fe_{0.2}O_{3-δ}+Co₃O₄ composite electrode for it-sofcs with improved electrical conductivity and catalytic activity,” *Electrochemistry Communications*, vol. 13, no. 2, pp. 197–199, 2011.
- [57] S. O. Lee, D. Lee, I. Jung, D. Kim, S.-H. Hyun, J. Kim, and J. Moon, “Ceria interlayer-free Ba_{0.5}Sr_{0.5}Co_{0.8}Fe_{0.2}O_{3-δ}-Sc_{0.1}Zr_{0.9}O_{1.95} composite cathode on zirconia based electrolyte for intermediate temperature solid oxide fuel cells,” *International Journal of Hydrogen Energy*, vol. 38, no. 22, pp. 9320–9329, 2013.
- [58] Bamana, G., Miller, J. D., Young, S. L., & Dunn, J. B. (2021). Addressing the social life cycle inventory analysis data gap: Insights from a case study of cobalt mining in the Democratic Republic of the Congo. *One Earth*, 4(12), 1704-1714.
- [59] Banza Lubaba Nkulu, C., Casas, L., Haufroid, V., De Putter, T., Saenen, N. D., Kayembe-Kitenge, T., ... & Nemery, B. (2018). Sustainability of artisanal mining of cobalt in DR Congo. *Nature sustainability*, 1(9), 495-504.
- [60] Wilburn, D. R. (2012). Cobalt mineral exploration and supply from 1995 through 2013. US Department of the Interior, US Geological Survey.
- [61] Shedd, K. B., McCullough, E. A., & Bleiwas, D. I. (2017). Global trends affecting the supply security of cobalt. *Min. Eng*, 69(12), 37-42.
- [62] The Ultimate Guide to the Cobalt Market:2022, (N.d.-a). Retrieved from <https://www.cruxinvestor.com/articles/the-ultimate-guide-to-the-cobalt-market-2022>
- [63] Muralidharan N, Self EC, Nanda J, Belharouak I. Next-Generation Cobalt-Free Cathodes—A Prospective Solution to the Battery Industry’s Cobalt Problem. *Adv Energy Mater*. 2022;12:33–53. <https://doi.org/10.1002/9783527817252.ch3>

- [64] Muralidharan N, Self EC, Nanda J, Belharouak I. Next-Generation Cobalt-Free Cathodes—A Prospective Solution to the Battery Industry’s Cobalt Problem. *Transition Metal Oxides for Electrochemical Energy Storage*, in *Advanced Energy Materials*. 2022; Volume 12, Issue 9 <https://doi.org/10.1002/aenm.202103050>,
- [65] Tsurukawa, N., Prakash, S., & Manhart, A. (2011). Social impacts of artisanal cobalt mining in Katanga, Democratic Republic of Congo. Öko-Institut eV, Freiburg.
- [66] S. Akkurt, C. Sındıraç, T.Ö.Egesoy, G. Atıcı, E.Erisman, E.Erğen, and A.Büyükkaksoy, “Effects of electro spraying parameters on deposition of $\text{La}_{0.3}\text{Sr}_{0.7}\text{Fe}_{0.7}\text{Cr}_{0.3}\text{O}_{3-\delta}$ cathode layer on GDC”, *Int. Journal of Applied Ceramic Technology*, vol.20, Issue 3, pp.1327-2042, doi:10.1111/ijac.14303
- [67] Jaworek, A., & Sobczyk, A. T. (2008). Electro spraying route to nanotechnology: An overview. *Journal of Electrostatics*, 66(3–4), 197–219. doi:10.1016/j.elstat.2007.10.001
- [68] Wang, S., Zhang, J., Gharbi, O., Vivier, V., Gao, M., & Orazem, M. E. (2021), *Electrochemical Impedance Spectroscopy (EIS)*, Nature Reviews, Retrieved from: nature.com
- [69] Magar, H. S., Hassan, R. Y., & Mulchandani, A. (2021). Electrochemical impedance spectroscopy (EIS): Principles, construction, and Biosensing Applications. *Sensors*, 21(19), 6578. doi:10.3390/s21196578
- [70] Pumiglia, D., Massimiliano, D. P., Monforti Ferrario, A., McPhail, S., & Pylypko, S. (2022). Impedance-based solid oxide fuel cell testing as scalable and reliable quality control tool for cell and batch manufacturing: First findings. *E3S Web of Conferences*, 334, 04021. doi:10.1051/e3sconf/202233404021
- [71] Astm C20, “Standard Test Methods for Apparent Porosity, Water Absorption, Apparent Specific Gravity, and Bulk Density of Burned Refractory Brick and Shapes by Boiling Water 1 This international standard was developed in accordance with internationally recognized pri,” *ASTM Int.*, vol. 00, no. Reapproved 2015, pp. 20–22, 2017, doi: 10.1520/C0020-00R10.
- [72] Xia C, Liu M. Microstructures, conductivities, and electrochemical properties of $\text{Ce}_{0.9}\text{Gd}_{0.1}\text{O}_2$ and GDC–Ni anodes for low-temperature SOFCs. *Solid State Ionics*. 2002;152–153(153):423–430. doi:10.1016/S0167-2738(02)00381-8

- [73] Wang S, Kobayashi T, Dokiya M, Hashimoto T. Electrical and Ionic Conductivity of Gd-Doped Ceria. *Journal of The Electrochemical Society*. 2000;147(10):3606. doi:10.1149/1.1393946
- [74] Badwal, S. P., Fini, D., Ciacchi, F. T., Munnings, C., Kimpton, J. A., & Drennan, J. (2013). Structural and microstructural stability of Ceria – GADOLINIA electrolyte exposed to reducing environments of high temperature fuel cells. *Journal of Materials Chemistry A*, 1(36), 10768. doi:10.1039/c3ta11752a
- [75] Mazzoli, A., & Favoni, O. (2012). Particle size, size distribution and morphological evaluation of airborne dust particles of diverse woods by scanning electron microscopy and image processing program. *Powder Technology*, 225, 65–71. doi:10.1016/j.powtec.2012.03.033
- [76] Gupta, N., Biswal, A. Kr., Parthipan, A. Kr., Kaur, B., Sharma, B., Jacob, J., & Saha, S. (2019). Bicompartamental microparticles loaded with antibacterial agents for prolonging food shelf life. *Journal of Materials Science*, 54(13), 9729–9744. doi:10.1007/s10853-019-03577-7
- [77] Fritz, M., Körsten, S., Chen, X., Yang, G., Lv, Y., Liu, M., ... Fischer, C. B. (2022). High-resolution particle size and shape analysis of the first samarium nanoparticles biosynthesized from aqueous solutions via cyanobacteria *Anabaena cylindrica*. *NanoImpact*, 26, 100398. doi:10.1016/j.impact.2022.100398
- [78] Gadolinium Doped Ceria %10 Gd – Premium Powder, Fuel Cell Materials, (2022). Retrieved from fuelcellmaterials.com/products/powders/electrolyte-powders/electrolyte-gadolinium-doped/gadolinium-doped-ceria-10-gd-premium-powder/
- [79] H. Harris, W. Lautenberger, *Strategy of Experimentation*, E.I. Dupont de Nemours & Co. Inc. Short Course Notes, 1976.
- [80] H.D. Leigh, C.A. Towe, Use of a screening experimental design to develop a high Al₂O₃ casting slip, *Am. Ceram. Soc. Bull.* 66 (5) (1987) 786–789.
- [81] S. Kavalci, E. Yalamaç, and S. Akkurt, “Effects of boron addition and intensive grinding on synthesis of anorthite ceramics,” *Ceram. Int.*, vol. 34, no. 7, pp. 1629–1635, 2008, doi: 10.1016/j.ceramint.2007.07.007.
- [82] K.K. Hansen, Evaluation of LSF based SOFC cathodes using cone-shaped electrodes and EIS, *Solid State Ionics* 344 (2020) 115096.

- [83] F.S. Baumann, J. Fleig, H.-U. Habermeier, J. Maier, “Impedance spectroscopic study on well-defined (La,Sr)(Co,Fe)O_{3-δ} model electrodes”, *Solid State Ionics* 177(11) (2006) 1071-1081.
- [84] Rupp, G. M., Téllez, H., Druce, J., Limbeck, A., Ishihara, T., Kilner, J., & Fleig, J. (2015). Surface chemistry of La_{0.6} Sr_{0.4} CoO_{3-δ} thin films and its impact on the oxygen surface exchange resistance. *Journal of Materials Chemistry A*, 3(45), 22759-22769.
- [85] Peters, C., Weber, A., & Ivers-Tiffée, E. (2008). Nanoscaled (La_{0.5}Sr_{0.5})CoO_{3-δ} thin film cathodes for SOFC application at 500° C < T < 700° C. *Journal of the Electrochemical Society*, 155(7), B730.
- [86] Karageorgakis, N. I., Heel, A., Bieberle-Hütter, A., Rupp, J. L., Graule, T., & Gauckler, L. J. (2010). Flame spray deposition of La_{0.6}Sr_{0.4}CoO_{3-δ} thin films: Microstructural characterization, electrochemical performance and degradation. *Journal of power sources*, 195(24), 8152-8161.
- [87] Adler, S. B. (1998). Mechanism and kinetics of oxygen reduction on porous La_{1-x}Sr_xCoO_{3-δ} electrodes. *Solid State Ionics*, 111(1-2), 125-134.
- [88] Adler, S. B., Lane, J. A., & Steele, B. C. H. (1996). Electrode kinetics of porous mixed-conducting oxygen electrodes. *Journal of the electrochemical society*, 143(11), 3554.
- [89] Januschewsky, J., Ahrens, M., Opitz, A., Kubel, F., & Fleig, J. (2009). Optimized La_{0.6}Sr_{0.4}CoO_{3-δ} Thin-Film Electrodes with Extremely Fast Oxygen-Reduction Kinetics. *Advanced Functional Materials*, 19(19), 3151-3156.
- [90] Baumann, F. S., Fleig, J., Habermeier, H. U., & Maier, J. (2006). Impedance spectroscopic study on well-defined (La, Sr)(Co, Fe) O_{3-δ} model electrodes. *Solid State Ionics*, 177(11-12), 1071-1081.
- [91] Simrick, N. J., Bieberle-Hütter, A., Ryll, T. M., Kilner, J. A., Atkinson, A., & Rupp, J. L. M. (2012). An investigation of the oxygen reduction reaction mechanism of La_{0.6}Sr_{0.4}Co_{0.2}Fe_{0.8}O₃ using patterned thin films. *Solid State Ionics*, 206, 7-16.
- [92] Yang, Y. L., Chen, C. L., Chen, S. Y., Chu, C. W., & Jacobson, A. J. (2000). Impedance studies of oxygen exchange on dense thin film electrodes of La_{0.5}Sr_{0.5}CoO_{3-δ}. *Journal of the Electrochemical Society*, 147(11), 4001.
- [93] Stuart B. Adler *Chemical Reviews* 2004 104 (10), 4791-4844 DOI: 10.1021/cr020724o

- [94] Beatriz Molero-Sanchez, Paul Addo, Aligul Buyukaksoy, and Viola Birss “Performance Enhancement of $\text{La}_{0.3}\text{Ca}_{0.7}\text{Fe}_{0.7}\text{Cr}_{0.3}\text{O}_{3-\delta}$ Air Electrodes by Infiltration Methods”, *Journal of The Electrochemical Society*, 164 (10) F3123-F3130 (2017)
- [95] Beatriz Molero-Sanchez, Emilio Moran and Viola Birss “Rapid and Low-Energy Fabrication of Symmetrical Solid Oxide Cells by Microwave Methods” *ACS Omega* 2017, 2, 3716–3723